A Tale of Two Trees: Modeling Apical and Basal Tree Contribution to L2/3 V1 Pyramidal Cell Orientation Selectivity

Konstantinos-Evangelos Petousakis[1,2,*], Jiyoung Park[3,*], Athanasia Papoutsi[1], Stelios Smirnakis[3,+], Panayiota Poirazi[1,+]

[1]IMBB, FORTH, Heraklion, Crete, 70013, Greece

[2]Department of Biology, University of Crete, Heraklion, Crete, 70013, Greece

[3]Department of Neurology, Brigham and Women's Hospital and Jamaica Plain Veterans Administration Hospital, Harvard Medical School, Boston, MA, USA

+Corresponding authors: poirazi@imbb.forth.gr, msmirnakis@bwh.harvard.edu

[*]These authors contributed equally to this work

Pyramidal neurons, a mainstay of cortical regions, receive a plethora of inputs from various areas onto their morphologically distinct apical and basal trees. Both trees differentially contribute to the somatic response, defining distinct anatomical and possibly functional sub-units. To elucidate the contribution of each tree to the encoding of visual stimuli at the somatic level, we modeled the response pattern of a L2/3 V1 pyramidal neuron to orientation tuned synaptic input. Towards this goal, we used a morphologically detailed computational model of a single cell that replicates electrophysiological and two-photon imaging data. Our simulations predict a synergistic effect of apical and basal trees on somatic action potential generation: basal tree activity, in the form of either depolarization or dendritic spiking, is necessary for producing somatic activity, despite the fact that most somatic spikes are heavily driven by apical dendritic spikes. This model provides evidence for synergistic computations taking place in the basal and apical trees of the L2/3 V1 neuron along with mechanistic explanations for tree-specific contributions and emphasizes the potential role of predictive and attentional feedback input in these cells.

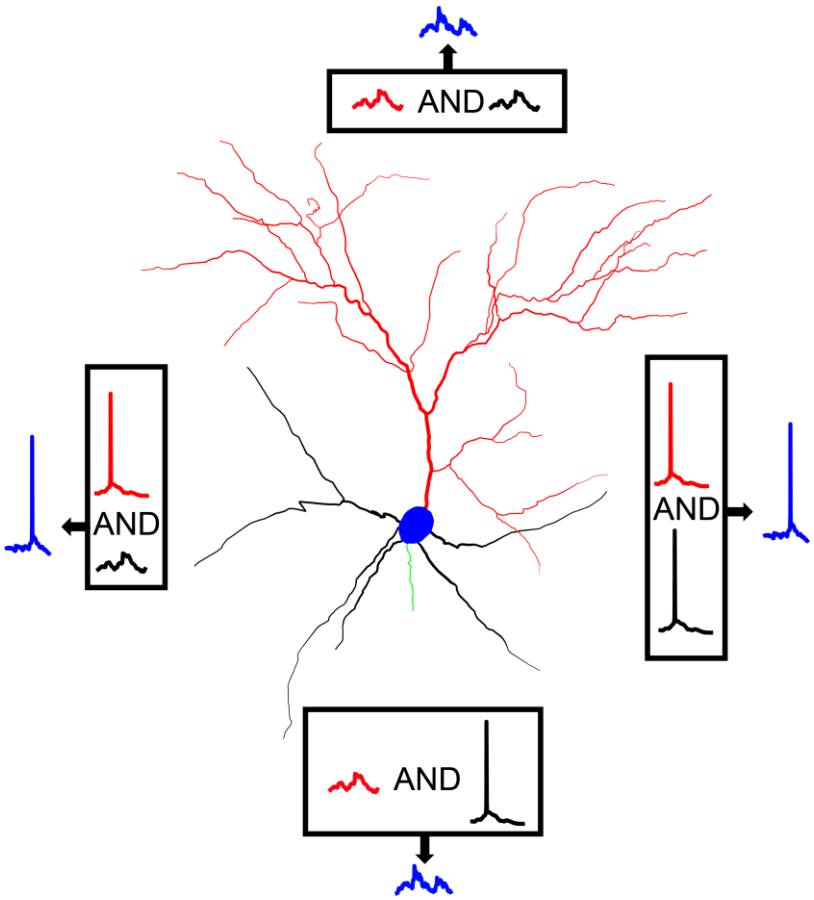

Abstract Figure. Graphical Representation of AP Generation in a L2/3 V1 Pyramidal Neuron Model*. Action potential generation requires the spatiotemporal coincidence of apical sodium spikes with either basal sodium spikes or significant basal depolarizations, allowing the neuron to respond to salient stimuli that may or may not be affected by attentional and/or predictive signals from higher-order areas.*

1. Introduction

In the primary visual cortex (V1), layer 2 and 3 (L2/3) pyramidal neurons conform to a stereotypical morphology characterized by separate apical and basal dendritic arbors. The apical tree consists of a thick apical trunk that extends into L1 and splits into an apical tuft. The basal tree consists of numerous dendritic segments, the majority of which sprout directly from the base of the soma, indicating that they can directly influence somatic output (Spruston, 2008). This compartmentalization of V1 neurons is also evident in the wiring diagram describing each tree: layer 4 (L4) and L2/3 pyramidal neurons synapse with basal

dendrites of L2/3 pyramidal neurons, providing them with feedforward input (Coogan & Burkhalter, 1990; Larkum, 2013). The apical dendrites of the L2/3 pyramidal neurons instead receive feedback input from higher order areas of the cortex (such as the secondary and tertiary visual cortices, lateromedial area and prefrontal cortex (Coogan & Burkhalter, 1990; Larkum, 2013), as well as orientation-tuned thalamocortical input (Chen et al., 2013; Cruz-Martín et al., 2014; Jia et al., 2010; Roth et al., 2015). These anatomical and connectivity features of the apical and basal trees, complemented by their distinct biophysical properties (Cho et al., 2008), shape both the local dendritic processing and the integration of the two input streams at the soma.

Few studies have undertaken the technically difficult task of measuring single spine tuning properties in the mouse visual cortex (Chen et al., 2013; Iacaruso et al., 2017; Jia et al., 2010). These studies have shown that single spines of L2/3 pyramidal neurons exhibit orientation selectivity, with synaptic orientation preferences varying even on the same branch (Iacaruso et al., 2017; Jia et al., 2010). These findings raise the question of how dendritic integration of sparse synaptic inputs along the apical and basal trees shape orientation tuning in L2/3 V1 pyramidal neurons.

The effect of synaptic input on neuronal output depends on the biophysical properties of dendritic branches. It has been found that individual dendritic segments of L2/3 neurons generate nonlinear regenerative responses, termed dendritic spikes, independently of the soma, making their exact contribution to somatic output unclear (Palmer et al., 2014; Smith et al., 2013). This could indicate that multiple dendritic segments need to be activated in order to generate a spike at the soma. On the other hand, it was recently proposed that strong, sparse inputs to the dendrites are sufficient to drive somatic output (Goetz et al., 2021).

Interestingly, although dendritic spikes in the apical tuft of L2/3 V1 pyramidal neurons influence orientation selectivity (Goetz et al., 2021; Smith et al., 2013), this orientation selectivity is robust to ablation of the apical tree (Park et al., 2019). Altogether, the above studies highlight the need to scrutinize the functional effect that synaptic inputs along the basal and apical dendritic arbors have on the soma towards a realistic theory of visual processing.

In this work, we used a detailed biophysical model of a L2/3 V1 pyramidal cell (Park et al., 2019), to tease apart the relative contributions of apical vs. basal dendritic trees in somatic orientation tuning. We start by examining the threshold and strength of dendritic non-linearities, which are found to vary along the apical and basal dendrites. By comparing model output to *in vivo* two-photon calcium fluorescence imaging data, we find that dendritic and somatic spontaneous activity patterns in the model adequately reproduce experimental data. We then simulate orientation tuning in our model and evaluate its responses to specific combinations of dendritic disparity and synaptic distributions. We find that the tuned output of the model does not always match the linear summation of tuned input, instead deviating towards orientation preferences more closely matching either the apical or basal mean orientation preference.

We continue by evaluating the dependence of somatic spikes on dendritic voltage-gated sodium channel conductances by performing just-in-time interventions that nullify sodium conductance on either the apical or basal tree prior to a somatic spike. We find that the majority of stimulus-driven somatic spiking activity is dependent on sodium spikes generated in the apical tree, suggesting that apical and basal trees contribute via different mechanisms to tuned somatic output. We investigate this further by examining the role of both specific

ionic (sodium channels) and synaptic (AMPA/NMDA) mechanisms in shaping orientation tuning. Results indicate that apical sodium channels are critical for proper neuronal tuning, while basal sodium channels do not play as significant a role. Conversely, AMPA and NMDA activity of both the apical and basal trees is required for orientation tuning at the level of the soma. A potential reason for this is that basal dendritic branches feature higher sodium spiking thresholds for similar length-normalized electrotonic length constant values compared to apical branches, reducing their propensity to generate sodium spikes compared to apical dendrites.

Overall, our simulations suggest a synergistic effect between apical and basal trees, as somatic spikes are only reliably produced when apical dendritic sodium spikes coincide with basal synaptically-driven depolarizations and/or spikes. In this manner, apical and basal dendrites contribute to neuronal function using different mechanisms, ionic or synaptic, which together drive action potential generation in this neuronal type.

2. Summary Methods

2.1. Model Description

The single neuron model is based on the L2/3 V1 pyramidal cell model of (Park et al., 2019) created in the NEURON simulation environment (Hines & Carnevale, 2001). As the model makes use of a variety of passive and active mechanisms (*Supplementary Tables 1-4*), its electrophysiological properties were validated against experimental data (Park et al., 2019). Neither the morphology nor the biophysical properties of the source model were altered, barring specific ion channel or synaptic mechanism conductance changes wherever specified (see Extended Methods for details). Apical stimulus-driven synaptic inputs have had a 10 ms

delay added, to better reflect experimental data on feedback synaptic inputs (Ju et al., 2020). Simulations with synchronous activation of the apical and basal synaptic inputs resulted in qualitatively similar results (data not shown). For a more detailed description of the model, see (Park et al., 2019) and Extended Methods, section 8.1.

2.2. Simulation Information

All simulations were performed on our High-Performance Computing Cluster (Rocks 7.0) with 624 cores and 3.328 TB of shared RAM under CentOS 7.4 OS (Papadopoulos et al., 2003), through the NEURON simulation environment (Hines & Carnevale, 2001). Model neuron output measurements were obtained at a sampling rate of 10 KHz (dt = 0.1 ms). Unless specified otherwise, voltage recordings from any section of the model (soma / dendrites) were performed at the midpoint of the respective section. Simulation duration was 2500 ms, with stimulus onset (where present) at t = 500 ms. For information on manipulations of biophysical properties for specific experiments, see Extended Methods, section 8.2. For details on specific simulation protocols, see Extended Methods, section 8.3.

2.3 Two-Photon Imaging

All experimental protocols were approved by Brigham and Women's Hospital (BWH) Institution Animal Care and Use Committee. Male and female wild-type (C57BL/6) mice were purchased from The Jackson Laboratory and bred for experiments. A total of 2 mice were used in these experiments, with recordings from 11 neurons used for data analysis. For details on chronic window implantation, sparse labeling and *in vivo* imaging methodology, see Extended Methods, section 8.4.

136

137 **2.4. Data Analysis**

138 Data analysis of both modeling and two-photon imaging experiments was performed through
139 Python 3.8+, using publicly available libraries as well as custom code. Analysis procedures
140 include methods for dendritic spike detection, quantification of dendritic non-linearities,
141 calculation of dendritic electrotonic length constants, analysis of two-photon imaging
142 recordings, processing of calcium fluorescence traces, detection of calcium events,
143 conversion of voltage traces into approximate calcium fluorescence traces, and comparison
144 of *in vivo* fluorescence data with converted model voltage traces. For specifics, see Extended
145 Methods, section 8.5.

146

147 **3. Results**

148 **3.1. The degree of non-linearity varies across basal and apical model dendrites**

149 To ensure the validity of our modeling approach, we first examined dendritic integration by
150 characterizing the sodium spike properties of all dendritic segments (*Figure 1A*), wherein a
151 specific number of synapses is synchronously activated by two pulses at 50 Hz while all other
152 compartments are modeled as passive ('I3P'; see Extended Methods, section 8.3.1), and the
153 response of each dendritic segment is assessed. Results show that the model can produce
154 realistic dendritic spikes (*Supplementary Figures 1C&D*), while the properties of the spiking
155 events vary between dendritic segments (*Figures 1B-D, Supplementary Figures 1A&B*). Both
156 apical and basal dendritic segments exhibit a large degree of variation in their spiking
157 thresholds (*Figures 1E&F;* threshold synapse count mean and standard deviations: basal
158 12.286±6.649 sodium, 51.429±13.179 NMDA; apical 14.442±13.825 sodium, 40.721±23.675

NMDA). Dendritic segments with high sodium spiking thresholds also tended to exhibit higher NMDA spiking thresholds. To quantitatively characterize the nonlinear behavior of each dendritic segment we used the Nonlinearity Relative to Linear Extrapolation (NRLE) metric (Behabadi et al., 2012), which is an estimate of the degree of non-linear dendritic integration within a specific branch (see Extended Methods, section 8.5.2). Results indicate that all dendritic segments of the model neuron exhibit non-linear input-output functions (*Figure 1D,* NRLE=1 denotes linear, NRLE<1 sublinear, and NRLE>1 supralinear), in line with experimental observations (Smith et al., 2013; Wilson et al., 2016). In addition, the NRLE values are relatively widely dispersed (values ranging from >1 to ~3.5), providing a large dynamic range of possible dendrite-level computations. The above results show that there is diversity in apical and basal dendritic integration that can be exploited to modulate orientation tuning. The above differences are, at least in part, due to the morphological and electrophysiological features of dendritic segments, as we found that the sodium spiking propensity varies as a function of dendritic segment volume and electrotonic constant (see *Figures 5C&D*).

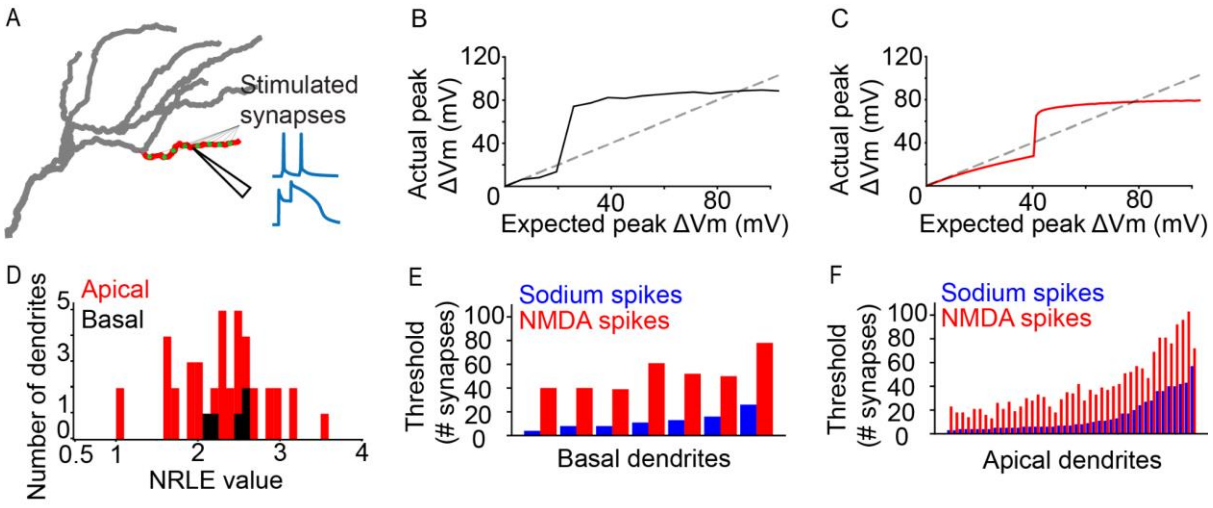

Figure 1. Dendritic Properties of a L2/3 V1 Neuron Model*. A. Graphical representation of the iterative paired-pulse protocol. Green dots represent allocated synapses. Synapses were activated only within the designated (red) dendritic segment, with all other segments being passive. We record the voltage response of the dendritic*

segment with NMDA channels disabled or enabled, acquiring information on dendritic sodium and NMDA spikes, respectively. B. Example of an "expected vs. actual plot", showing the response produced by a single basal dendritic segment (solid black line) as a result of voltage-gated sodium channel activity elicited through simultaneous activation of 1 to 200 AMPA synapses. The dashed black line indicates the expected dendritic response assuming a linear dendrite. C. Same as B, but for an apical dendritic segment. D. NRLE value histogram for all apical (red) and basal (black) dendritic segments. E. Bar plot of per-dendrite nonlinearity thresholds for all basal dendritic segments, sorted by the sodium spike thresholds. Note that NMDA spike thresholds largely follow the sodium spike threshold increase. F. As E, for all apical dendritic segments.

3.2. Model neuron features robust orientation tuning

Given the diverse integration properties of basal and apical dendrites in our model cell, we sought to assess their functional cooperation when receiving a more realistic set of background- and stimulus-driven inputs. Stimulus driven synapses were modeled with individual orientation preferences (Jia et al., 2010; Park et al., 2019), leading them to exhibit different firing rates depending on the orientation of the presented stimulus (for details, see Extended Methods, section 8.1). As dictated by experimental data (Chen et al., 2013), background-driven synapses comprise the majority of inputs to the model, although they are activated at lower rates than stimulus-driven synapses (see Extended Methods, section 8.1). To validate their impact on somatic output, we compared the simulated spontaneous activity with *in vivo* calcium two-photon fluorescence imaging data (see Extended Methods, section 8.5.7 and *Supplementary Figure 2*). Although this approach has its limits, it allows us to use two-photon imaging data to increase model reliability. We found that spontaneous activity patterns in the model are very similar to those seen in two-photon calcium imaging data (*Supplementary Figures 2E&F*).

Next, we combined stimulus-driven and background-driven activity to derive the orientation tuning curve of the model neuron (see Extended Methods, section 8.3.3). We focused on the biologically plausible model (see Extended Methods, section 8.1), whereby the distribution of tuned synaptic inputs onto the basal and apical trees is in line with experimentally reported values (60% vs 40%, respectively; DeFelipe & Fariñas, 1992). The resulting orientation tuning curve (preferred orientation firing rate: 1.55±0.3 Hz, orthogonal orientation firing rate: 0.21±0.12 Hz, OSI 0.77±0.11, tuning width 44±9.17°; *Figure 2A*) indicates that the model neuron is well-tuned (OSI>0.2, tuning width<80°; see Extended Methods, section 8.3.3), in agreement with our prior work using the original version of this model (Park et al., 2019).

Having established the orientation tuning of our model cell, we tried to disentangle the effects of the apical and basal trees by introducing dendritic disparity (*Figure 2B;* see Extended Methods, section 8.3.4). We used the disparity protocol, in which the apical and basal trees are tuned to different orientations: the apical tree features synaptic orientation preferences sampled from a Gaussian distribution with a mean of 0°, whereas the basal tree uses the same method, but with a different mean (0° - 90°, in steps of 10°). The expected orientation preference of the model neuron is calculated using Euler's Formula, which assumes that synapses contribute to overall orientation preference in a linear fashion (for details, see Extended Methods, section 8.3.4). We found that the model neuron diverges from the expected orientation preference (linear summation of synaptic inputs) and exhibits a bias towards the preferred orientation of the basal tree. This is an example of *basal dominance* (*Figure 2D*) and was previously observed using the original version of the model used here (Park et al., 2019). Of note, the model neuron did not exhibit adequate tuning (i.e. 20% or more of neurons featured OSI<0.2 or tuning width >80°; see Extended Methods, section 8.3.3)

beyond a dendritic disparity of 50°.

To assess whether this result depends on the particular synaptic distribution used, we repeated the experiment using two different synaptic distribution profiles – the “inverse biologically plausible” (40% on the basal tree, 60% on the apical tree) and “even” (50% on both trees) models (see Extended Methods, section 8.1). We found that, indeed, the deviation from expectation displayed by the neuron appears to be decreased in the “even” model, and is clearly reversed in the “inverse biologically plausible” model. Similar to the “biologically plausible” model, these two models did not feature adequate tuning past 50° of dendritic disparity. Overall, the observed deviation from expectation indicates that apical and basal synaptic inputs are not linearly combined, but rather interact in a non-linear manner to produce somatic output. This interaction is influenced by the synaptic distribution along the two dendritic trees, as well as their mean synaptic orientation preferences.

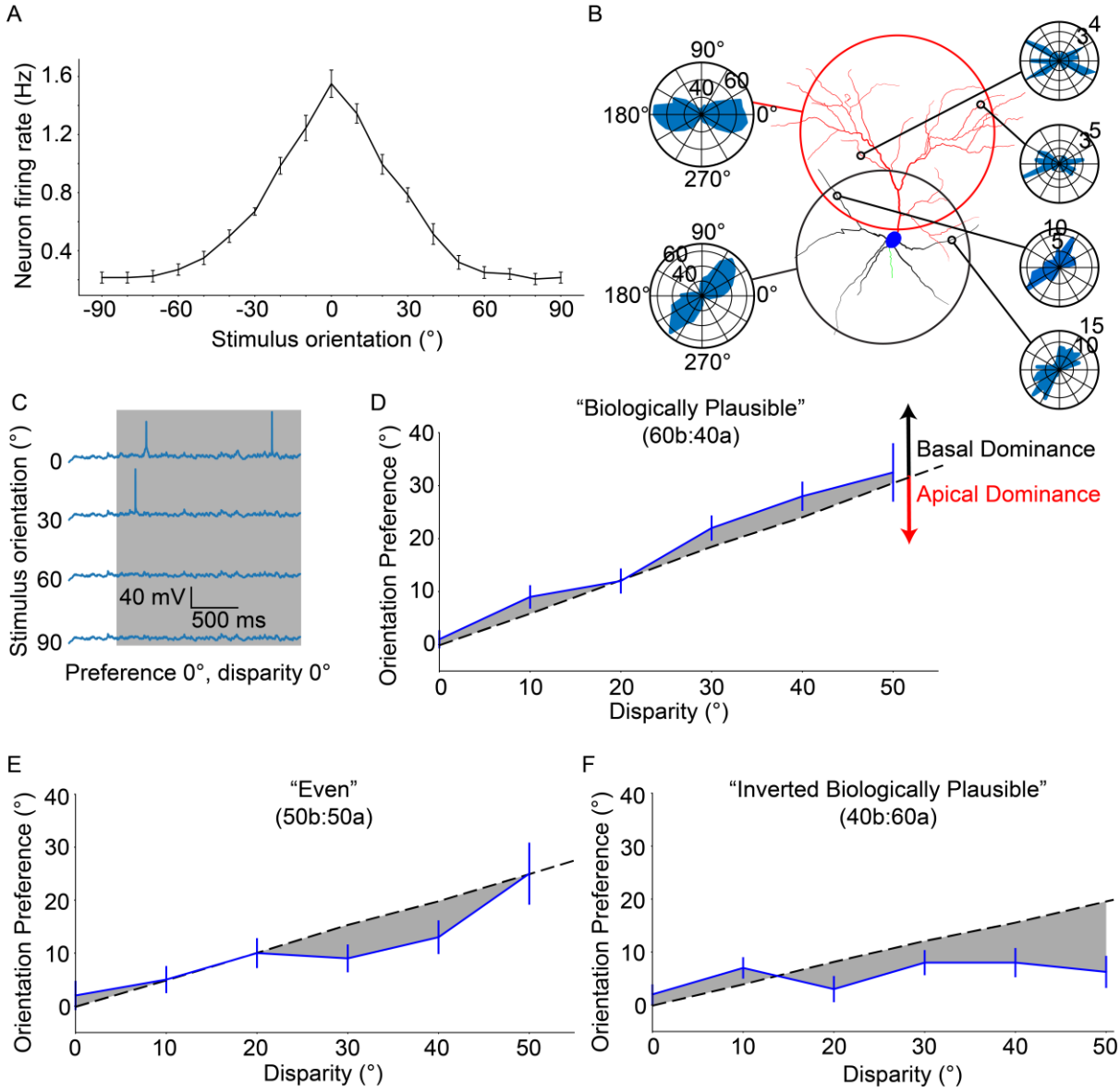

Figure 2. Neuronal Orientation Preference is Robust and Resists Dendritic Tuning Disparity*. A. Orientation tuning curve for the "biologically plausible" model. B: Example from a configuration of a model neuron set to a disparity of 40°. Right-side polar plots display the distribution of synaptic orientation preferences for the indicated dendritic segments. Left-side polar plots display the distribution of synaptic orientation preferences for the apical (top) and basal (bottom) dendritic trees. C: Example voltage traces recorded at the soma of a model neuron from (A). Note the clearly different responses between the preferred orientation (0°) and all others. D: Orientation preference plot for the "biologically plausible" model featuring various degrees of disparity. Grey dashed line denotes the expected orientation preference per degree of disparity. Black and red arrows point in the direction of basal and apical dominance, respectively. E: As D, but for the "even" model. Note that dominance has shifted from the basal domain towards the apical domain. F: As D, but for the "inverted biologically plausible" model.*

This configuration clearly features apical dominance. Error bars: Standard error of the mean, for all panels.

3.3. Apical Sodium Spikes are the Primary Driver of Neuronal Output

The previous results show that orientation tuning emerges from non-linear interactions between apical and basal trees. To elucidate the contribution of each tree in orientation tuning, we selectively interrupt specific aspects of their operation and assess the effect of the intervention on somatic tuning. We start by selectively and precisely modifying the sodium spiking activity of each dendritic tree, while controlling for the type of input received (stimulus-driven vs background-driven). Specifically, we use the ionic intervention protocol (see Extended Methods, section 8.3.6) to remove the sodium-induced depolarization that is provided by either the apical or the basal tree, just before the generation of a somatic spike.

We start by using a control version of the "biologically plausible" model ("Control background") and a preferred (0°) stimulus (case #1). In this condition, both stimulus-driven and background-driven synapses are active, and most synapses (60%; both stimulus-driven and background-driven) are allocated on the basal tree. For every somatic spike, we perform the intervention protocol and categorize the spike as either: "apically-driven" (dependent on the presence of apical sodium conductances), "basally-driven (dependent on the presence of basal sodium conductances) or "cooperative" (dependent on the presence of both apical and basal sodium conductances) (*Figure 3A*). We find that the majority of somatic spikes are dependent on apical sodium conductance (N = 131 spikes; apically-driven 76.51±10.21%, basally-driven 9.61±5.03%, cooperative 13.89±11.22%; *Figure 3B)*, which is surprising, considering the proximity of the basal dendrites to the soma, as well as the salient nature of the feedforward, visually-evoked inputs received by the basal tree. These somatic events are

270 a mix of stimulus-driven and background-driven input. In order to separate the two, we
271 changed the orientation of the stimulus being presented to 90° (i.e. orthogonal to the
272 orientation preference of the neuron), rendering the vast majority of stimulus-driven
273 synapses inactive, while keeping background-driven synapses active as normal (case #2). We
274 found that the resulting percentages are similar to the previous condition (N = 25 spikes;
275 apically-driven 71.07±31.56%, basally-driven 17.5±22.5%, cooperative 1.43±4.29%; *Figure*
276 *3D)*, indicating that the dependence of somatic spiking activity on dendritic sodium
277 conductance does not significantly differ between instances of stimulus-driven and
278 background-driven activity.

279 However, it is possible that background-driven synapses are actually the ones that determine
280 somatic spiking. While firing at low rates (0.11 Hz vs 0.3 Hz for stimulus-driven; see Extended
281 Methods, section 8.1), these synapses are vastly more numerous compared to stimulus-
282 driven synapses (75% versus 25% of total synapses). To test this possibility, we equalized the
283 contribution of background-driven synapses to apical and basal tree outputs, by introducing
284 a new condition ("Evenly distributed background") whereby the model is configured as in case
285 #1 (i.e. "biologically plausible" model), but the distribution of *background-driven synapses* is
286 the same on both trees (i.e. excitatory: 50% apical, 50% basal; inhibitory: 46.5% apical, 46.5%
287 basal, 7% soma). In this way, we ensure that the greater proportion of background-driven
288 synapses on the basal tree is no longer a confounding factor. Presenting a stimulus of the
289 preferred orientation (0°) under these conditions (case #3), we find that the resulting
290 percentages (N = 156 spikes; apically-driven 85.08±7.34%, basally-driven 5.15±6.72%,
291 cooperative 9.78±8.17%; *Figure 3C)* are similar to those seen in case #1, indicating that the
292 distribution of background-driven synapses does not significantly affect somatic spike

generation.

By changing the orientation of the presented stimulus to 90° for this altered model configuration, we can also evaluate whether the same conclusion holds for background-driven spikes (case #4). Indeed, the results (N = 42 spikes; apically-driven 85.83±29.83%, basally-driven 2.5±7.5%, cooperative 1.67±5.0%; *Figure 3E)* are not significantly different from those seen in case #2. These simulations predict that somatic spike generation reliably depends on apical sodium conductance, a seemingly counterintuitive finding, as feedforward stimulus-driven input reaches mostly the basal tree and not the apical tree.

To gain more insight into these findings, we looked at the spatiotemporal evolution of voltage through different apical and basal paths during the occurrence of an apically- or basally-driven spike (*Supplementary Figure 6*). For heavily branching apical dendrites, input summation and/or voltage propagation in one segment along the path exceeds the sodium spiking threshold, leading to a cascade of dendritic sodium spikes both in the direction of the soma as well as towards any terminal dendrites that did not yet generate sodium spikes of their own (e.g. *Supplementary Figure 6H;* dendritic sodium spiking does not originate from the terminal segment, but propagates to it). The lack of extensive branching on the basal dendrites, on the other hand, renders them less predictable in terms of sodium spiking activity (e.g. *Supplementary Figure 6C*). Although the intervention experiments are required in order to decisively determine the origin of each somatic spike, the temporal precedence of dendritic sodium spiking reliably indicates which tree drives somatic spiking activity (e.g. compare *Supplementary Figure 6B vs 6C and 6E vs 6F*).

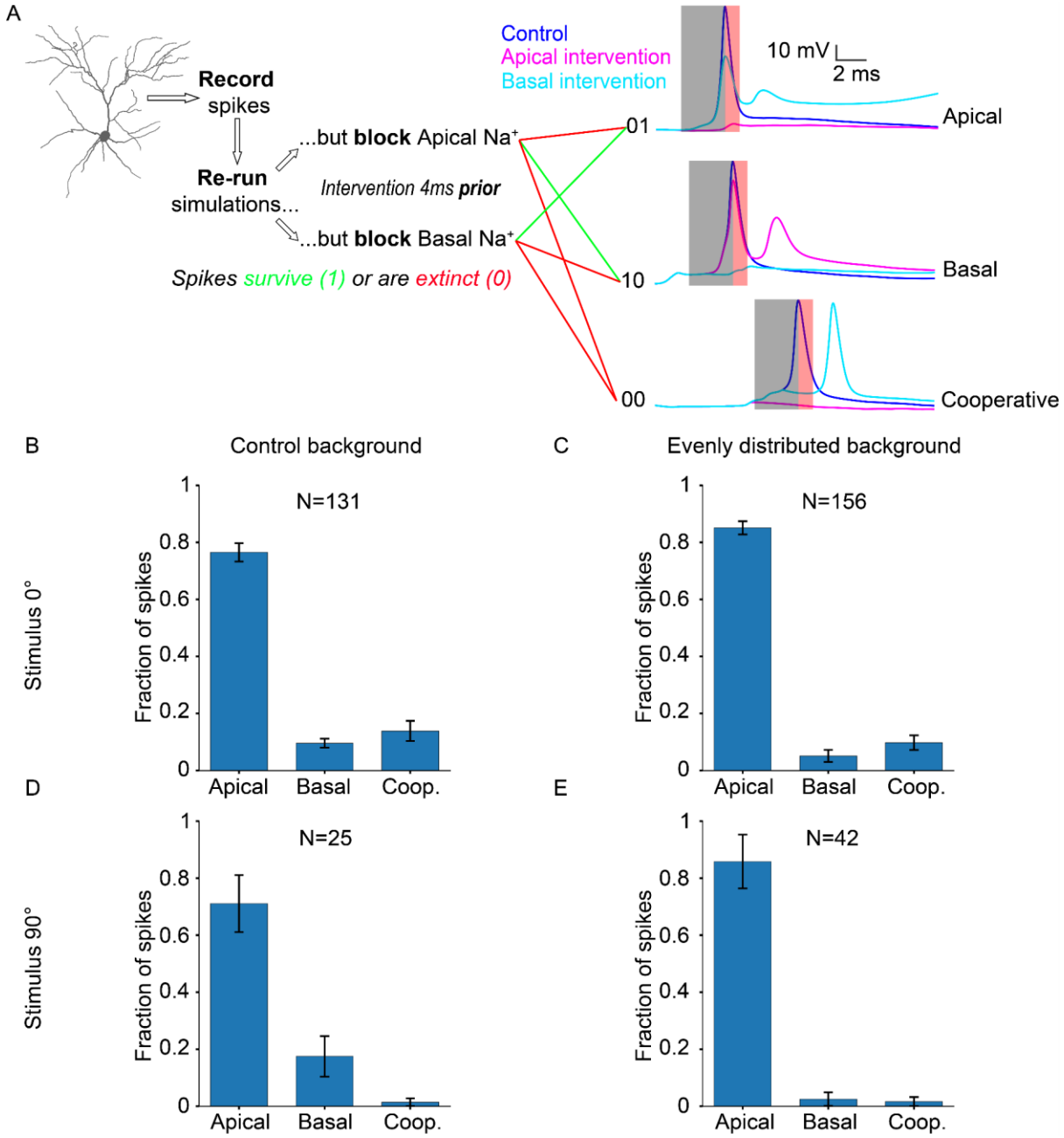

315

316 ***Figure 3. Neuronal Output Relies Disproportionately on Apical Sodium Conductance****. A: Diagram describing the*
317 *ionic intervention protocol, with example traces on the right. Shaded areas on the traces denote the pre-spike*
318 *(grey) and post-spike (red) intervention time windows. B: Somatic spike dependence on dendritic sodium*
319 *conductance for the "biologically plausible" model with a stimulus of 0° (preferred orientation). C: Same as B, but*
320 *background synapses are evenly distributed across the apical and basal dendritic trees, while stimulus-driven*
321 *synapses follow the "biologically plausible" (60% basal, 40% apical) model. D: Somatic spike dependence on*
322 *dendritic sodium conductance for the "biologically plausible" model with a stimulus of 90° (orthogonal/non-*
323 *preferred orientation). E: Same as D, but background synapses follow the "even" model (evenly distributed), while*

stimulus-driven synapses follow the "biologically plausible" (60% basal, 40% apical) model. "N" is the total number of spikes for each condition. Error bars: Standard error of the mean, for all panels.

3.4. Apical and Basal Dendrites Influence Somatic Tuning via Different Mechanisms

The previous results are counter-intuitive: although we would expect both apical and basal dendritic segments to contribute to somatic spiking, the contribution of the apical tree overshadows that of the basal tree, at least with respect to the role of sodium conductances. However, as indicated by our results in *Figure 2D*, the basal tree, being the bearer of the majority of feedforward inputs, has a dominant role in orientation tuning. Thus, we assume that the basal tree exerts its influence via a different mechanism. To assess the veracity of this assumption, we performed a series of experiments aimed at evaluating the impact of ionic (see Extended Methods, sections 8.2.1 and 8.3.6) and synaptic (see Extended Methods, sections 8.2.2, 8.2.3 and 8.3.7) mechanisms on neuronal orientation tuning, using the biologically plausible model (see Extended Methods, section 8.3.2).

First, we assess the tuning characteristics of the neuron when stimulus-driven input is removed from either the apical or the basal tree (see Extended Methods, section 8.2.3), and compare it with the control case. We find that the neuron remains tuned in all cases, albeit with significantly decreased OSI values (dependent two-sample t-test, control vs basal: $p \approx 0.000037$; control vs apical: $p \approx 0.000007$) (*Figure 4A*). Removal of apical stimulus-driven input has a much smaller effect on tuning than removal of basal input (dependent two-sample t-test, apical vs basal: $p \approx 0.0095$), which is in line with our previous findings (Park et al., 2019).

Next, we use the synaptic intervention protocol to selectively reduce synaptic (AMPA and NMDA) weights by 50% on either the apical or basal tree for a brief time only, and only when

a somatic spike is about to occur (see Extended Methods, section 8.3.7). We find that somatic tuning is completely abolished when manipulating the basal but not the apical synaptic weights, although tuning is significantly affected by loss of apical inputs as well (*Figure 4B*) (dependent two-sample t-test, control vs apical: $p \approx 0.00065$). These results indicate that synaptic input from the basal tree is critical for orientation tuning, while apical tree synaptic inputs play a less important role.

Finally, we assess the impact of sodium conductance nullification (as in Fig. 3), this time on orientation tuning rather than somatic spiking. In line with our previous results (Fig. 3), we find that sodium conductance nullification in the apical tree completely abolishes orientation tuning (*Figure 4C*) while the same manipulation in the basal tree has no impact on tuning (dependent two-sample t-test, control vs basal: $p \approx 0.24125$).

3.4.1 Sensitivity Analysis

To assess whether the above findings are robust to biologically-relevant variability in the conductance values of sodium channels, we performed a sensitivity analysis whereby we reduced the sodium conductance only in the apical tree by either 5% or 10% (*Supplementary Figure 7*). For a decrease of 5%, we found that elimination of the apical but not the basal sodium component results in total loss of tuning (dependent two-sample t-test, control vs basal p-value: 0.32549). Importantly, in this scenario the apical tree remains the primary driver of somatic activity as the majority of somatic spikes are apically driven (*Supplementary Figure 7A,* N = 345 spikes; 60±15% of spikes are apically-driven, 30±18% are basally-driven, and 10±8% of spikes are cooperatively-driven, for details on the characterization of spiking activity, see Results, section 3.3). However, a 10% decrease in the apical sodium conductance

370 results in total loss of tuning when either the apical or the basal sodium component is
371 eliminated (*Supplementary Figure 7B*). In this case, a large number of spikes are completely
372 lost (N = 190 spikes vs 345), and out of the remainder, 41±25% are apically-driven, 48±28%
373 are basally-driven, and 11±12% are cooperatively-driven. We further compare these two
374 conditions (5% and 10% reduction) with one where the apical sodium conductance is
375 unchanged (*Supplementary Figure 7C,* identical to *Figure 4C*). Similarly to the results seen in
376 the 5% reduction, elimination of the apical - but not the basal - sodium component results in
377 total loss of tuning (dependent two-sample t-test, control vs basal p-value: 0.24125). In this
378 case, 80±9% of spikes are apically-driven, 13±8% are basally-driven, and 7±4% of spikes are
379 cooperatively-driven. Notably, the number of spikes is drastically higher in this condition (N =
380 885 spikes in the unchanged condition vs. N = 345 for the 5% reduction and N = 190 for the
381 10% reduction).

382 The above simulations show that, as expected, the reduction in apical sodium conductance
383 results in a decrease of the overall spiking rate of the neuron (number of spikes: 885 in the
384 unchanged condition, 345 for the 5% reduction, and 190 for the 10% reduction). Even so,
385 decreasing apical sodium conductance by 5% failed to negate its role in somatic spike
386 generation, with the apical tree remaining the primary contributor (60±15% of spikes were
387 apically-driven vs 30±18% basally-driven; *Supplementary Figure 7A*). A decrease of 10%,
388 however, exerts greater influence as an ever-larger number of apically-driven spikes are lost,
389 shifting the percentages to a more even distribution between apically-driven and basally-
390 driven (41±25% vs 48±28%, respectively; *Supplementary Figure 7B*). Of note, in this particular
391 case the neuronal firing rate is well below the experimentally-relevant range, suggesting that
392 such a reduction is not physiological (see *Supplementary Figure* 7A vs. 7B). Overall, our

sensitivity analysis suggests a greater-than-expected contribution of apical sodium non-linearities in somatic spike generation. This finding is in line with experimental work showing that L2/3 V1 neurons can produce spikes even in the absence of feedforward (i.e. basal stimulus-driven) activity (Keller et al., 2020).

Overall, our simulations predict that apical sodium channels are necessary for both spike generation in general (*Figure 3)* as well as for orientation tuning in particular (*Figure 4C).* Additionally, AMPA and NMDA activity is necessary for both apical and basal trees (*Figures 4A, 4B)*. This means that the apical tree most likely exerts its influence on somatic spiking via sodium-mediated spiking, whereas the basal tree mostly utilizes AMPA- and NMDA-driven depolarizations, rather than sodium spikes.

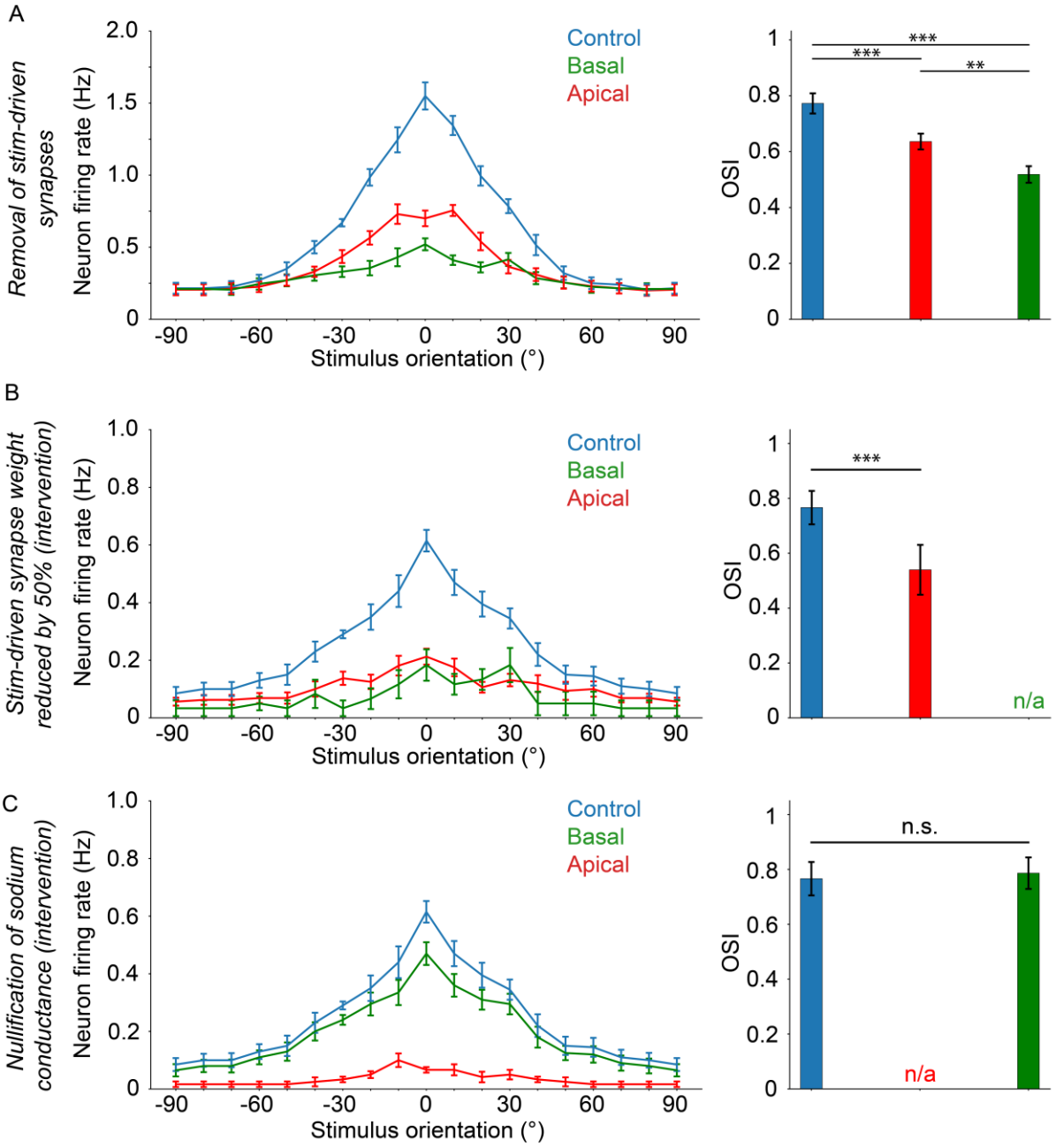

Figure 4. Orientation Tuning Critically Depends on Apical Sodium Conductance and AMPA/NMDA Activity. *A: Orientation tuning curves (left) and mean OSI values (right) for the experiment where stimulus-driven synapses are completely absent on either the apical ("apical target"; red) or basal ("basal target"; green) tree. B: Selective reduction of stim-driven synaptic (AMPA/NMDA) weights by 50% 30 ms prior to somatic spike occurrence (lasting up to 10 ms after the pre-recorded somatic spike timing), on either the apical (apical target; red) or basal (basal target; green) tree. C: Nullification of sodium conductances 3 ms prior to somatic spike occurrence (lasting up to 1 ms after the pre-recorded somatic spike timing), on either the apical (apical target; red) or basal (basal target; green) tree. Error bars: Standard error of the mean, for all panels. If present, "n/a" denotes a lack of orientation*

tuning for that specific experimental setup. Stars denote statistical significance at a significance level (α) of 0.05 (*), 0.01 (**) or 0.001 (***), whereas "n.s." stands for "no statistically significant difference", i.e. p-value ≥ α. Dependent two-sample t-tests were used in all cases.

3.5. Tree-Specific Morphological and Electrophysiological Properties Influence Dendritic and Somatic Behavior

Our simulations predict that apical and basal dendritic segments exert causal influence on somatic spike generation via separate mechanisms. In an attempt to explain these differences in contribution, we looked at the anatomical and electrophysiological properties of the two types of dendrites (apical/basal). Specifically, we searched for links between anatomical/electrophysiological properties of dendrites and (a) signal attenuation or (b) dendritic excitability (number of synapses required to drive a local sodium spike, or "threshold"; see also *Extended Methods,* section 8.5.9 for details).

To ensure a fair comparison among different dendritic branches, we induced a 20 mV local EPSP (actual amplitudes: 19.78 ± 0.98 mV) and assessed its attenuation at the soma (see Extended Methods, section 8.5.9). We found that EPSP attenuation is greater in apical versus basal dendritic segments of similar length (*Figure 5A;* p-value 0.000002), diameter (*Figure 5B;* p-value 0.005864) or volume (data not shown; p-value 0.000001). When normalized by distance from the soma (*data not shown*; p-value 0.42941), dendritic path volume (data not shown; p-value 0.027934), or electrotonic constant (data not shown; p-value 0.666959), EPSP attenuation did not significantly differ between apical and basal dendritic segments. We also examined the relationship between apical vs. basal EPSP attenuation in respect to high apical dendrite branching order (>3), as well as high apical dendrite distance from the soma (>182.7

435 µm). We found no significant difference between apical and basal dendrite EPSP attenuation
436 in respect to high apical dendrite branching order (*Supplementary Figure 8D*; apical
437 attenuation: 16.59±3.18 mV, basal attenuation: 13.96±2.8 mV, p-value 0.0956). A statistically
438 significant difference did emerge in the case of EPSP attenuation in respect to high apical
439 dendrite distance from the soma (*Supplementary Figure 8C*; apical attenuation: 17.64±1.84
440 mV, basal attenuation: 13.96±2.8 mV, p-value 0.0312) if an outlier was removed from the
441 basal dendrite attenuation data (see *Extended Methods,* section 8.5.10 for details).

442 We repeated this analysis for dendritic sodium spikes (*Supplementary Figure 8*) and found
443 similar results: spike attenuation is greater in apical versus basal dendritic segments, when
444 comparing apical and basal dendritic segments of approximately equivalent length
445 (*Supplementary Figure 8B;* p-value 0.000097), diameter (*Supplementary Figure 8A;* p-value
446 0.00646) or volume (data not shown; p-value 0.000002). There was no significant difference
447 in spike attenuation between apical and basal dendritic segments when controlling for
448 distance from the soma (data not shown; p-value 0.768547), dendritic path volume (data not
449 shown; p-value 0.061389), or electrotonic constant (data not shown; p-value 0.396982). As
450 above, we also examined dendritic spike attenuation at the soma in respect to high apical
451 dendrite branching order and high apical dendrite distance from the soma. There was no
452 significant difference between attenuation for apical vs basal sodium spikes in respect to
453 branching order (*Supplementary Figure 8F*; apical attenuation: 64.93±26.28 mV, basal
454 attenuation: 59.39±5.8 mV, p-value 0.2894), but a significant difference was present when
455 comparing attenuation in respect to distance from the soma (*Supplementary Figure 8E*; apical
456 attenuation: 70.94±22.85 mV, basal attenuation: 59.39±5.8 mV, p-value 0.0336), excluding an
457 outlier from the basal tree (see *Extended Methods,* section 8.5.10 for details).

The above suggest that signals originating in apical vs. basal dendritic segments with similar morphological characteristics (length, diameter, volume), attenuate more than those originating in basal dendritic segments. This is partly because most apical dendrites are located further away from the soma compared to basal dendrites: comparison of EPSP and sodium spike attenuation in respect to distance from the soma yields statistically significant differences between basal and distant apical dendrites (*Supplementary Figure 8C&E*).

Finally, we also examined the relationship between dendritic sodium spiking thresholds and the morphological and electrophysiological parameters stated previously. We found that dendritic sodium spiking thresholds are significantly lower for apical versus basal dendritic segments with approximately equivalent values of the electrotonic constant (*Figure 5C;* p-value 0.001585), but this relationship is reversed for dendritic segments with similar volume (*Figure 5D*; p-value 0.000002). On the contrary, apical and basal dendritic segments featuring similar distances from the soma (data not shown; p-value 0.320436), dendritic path volume (data not shown; p-value 0.418108), length (data not shown; p-value 0.407686) or diameter (data not shown*;* p-value 0.592490) did not exhibit significant differences in their sodium spiking thresholds.

Taken together, this analysis shows that - as expected - the attenuation of signals originating in morphologically and electrophysiologically equivalent dendritic segments is significantly larger for apical vs. basal dendrites, likely because most apical dendrites are located further away from the soma. However, the threshold for inducing sodium spikes in apical dendritic segments is significantly smaller compared to basal dendritic segments of similar electrotonic isolation (as indicated by their electrotonic constant), making it easier to drive such spikes in the apical compared to the basal tree. These findings provide a more intuitive explanation of

481 the greater role of sodium conductances in the apical vs. basal trees of our model neuron.

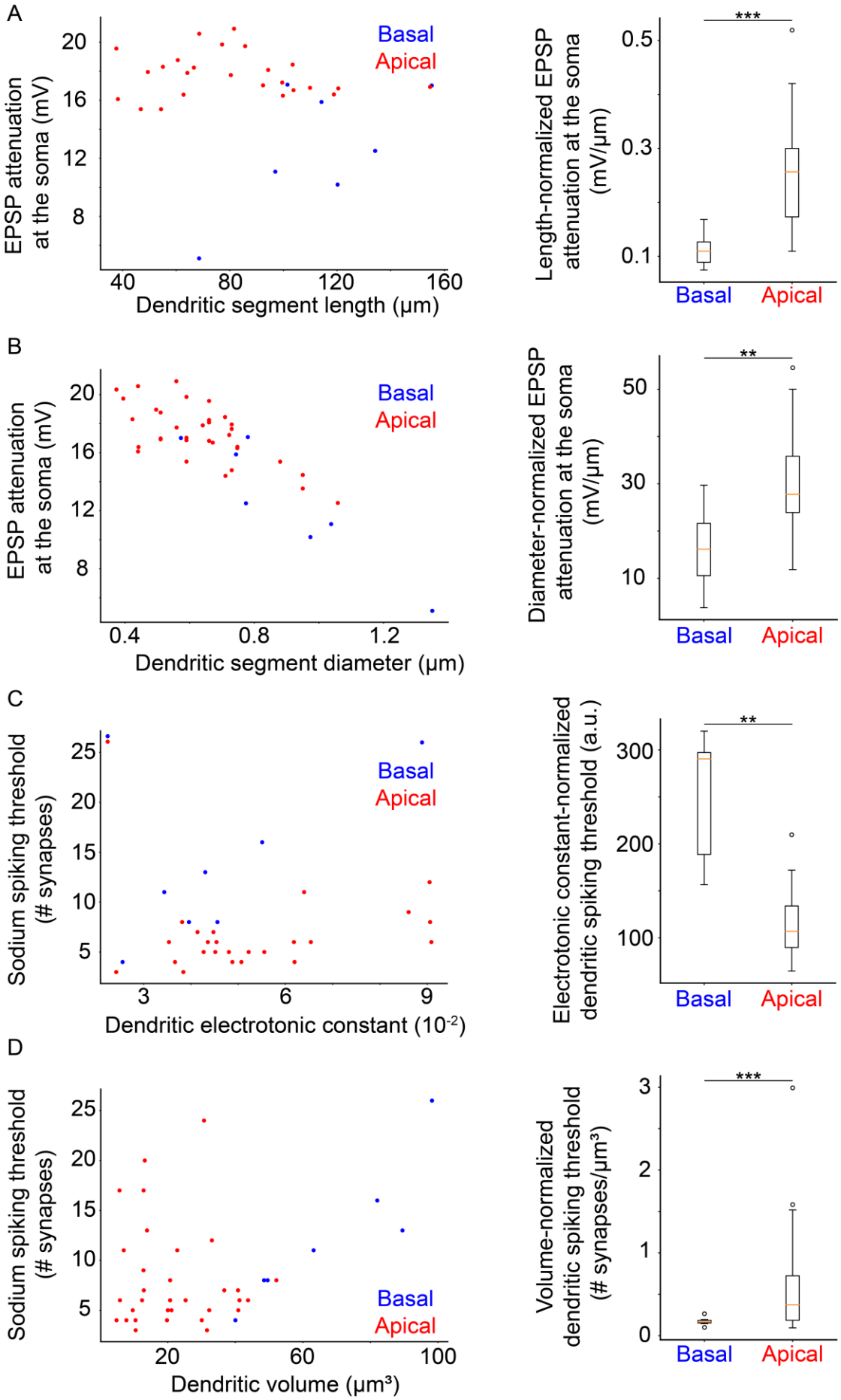
A
EPSP attenuation at the soma (mV)
20
16
12
8
40
80
120
160
Dendritic segment length (μm)
Basal
Apical
Length-normalized EPSP attenuation at the soma (mV/μm)
0.5
0.3
0.1
***
Basal
Apical
B
EPSP attenuation at the soma (mV)
20
16
12
8
0.4
0.8
1.2
Dendritic segment diameter (μm)
Basal
Apical
Diameter-normalized EPSP attenuation at the soma (mV/μm)
50
30
10
**
Basal
Apical
C
Sodium spiking threshold (# synapses)
25
20
15
10
5
3
6
9
Dendritic electrotonic constant (10-2)
Basal
Apical
Electrotonic constant-normalized dendritic spiking threshold (a.u.)
300
200
100
**
Basal
Apical
D
Sodium spiking threshold (# synapses)
25
20
15
10
5
20
60
100
Dendritic volume (μm³)
Basal
Apical
Volume-normalized dendritic spiking threshold (# synapses/μm³)
3
2
1
0
***
Basal
Apical

482

483 ***Figure 5. Dendritic Morphological and Electrophysiological Properties Affect both Local and Somatic Behavior.***
484 *A: Left: Attenuation of a 20 mV dendritic EPSP (measured at the soma) as a function of dendritic segment length.*
485 *Right: Comparison of length-normalized EPSP attenuation at the soma between apical and basal dendritic*
486 *segments. Apical dendritic segments feature greater attenuation. B: Left: Attenuation of a 20 mV dendritic EPSP*
487 *(measured at the soma) as a function of dendritic segment diameter. Right: Comparison of diameter-normalized*
488 *EPSP attenuation at the soma between apical and basal dendritic segments. Apical dendritic segments feature*
489 *greater attenuation. C: Left: Dendritic sodium spiking thresholds as a function of the dendritic electrotonic*
490 *constant (ELC). Right: Comparison of ELC-normalized sodium spiking thresholds between apical and basal*
491 *dendritic segments. Apical dendritic segments feature lower thresholds. D: Left: Dendritic sodium spiking*
492 *thresholds as a function of dendritic volume. Right: Comparison of volume-normalized sodium spiking thresholds*
493 *between apical and basal dendritic segments. Apical dendritic segments feature greater thresholds, but also*
494 *much greater variability of thresholds. Stars denote statistical significance at a significance level (α) of 0.05 (*),*
495 *0.01 (**) or 0.001 (***), whereas "n.s." stands for "no statistically significant difference", i.e. p-value ≥ α.*
496

497 **4. Discussion**

498 In this work, we used a detailed computational model to delineate the dendritic constituents
499 of neuronal computation in L2/3 V1 pyramidal cells. We found that the model exhibits a wide
500 range of non-linear behavior at the dendritic segment level (*Figure 1*) and can mimic the
501 activity patterns of neurons under spontaneous conditions *in vivo* (*Supplementary Figure 2*).
502 The model neuron exhibits robust orientation tuning in response to tuned input (*Figure 2A*),
503 and under conditions of dendritic disparity, the model still remains robustly tuned (OSI < 0.2
504 and tuning width > 80°) for non-extreme dendritic disparity conditions (disparity ≤ 50°).
505 Importantly, the neuronal orientation preference deviates from the expected one (*Figure 2D-*
506 *F*), indicating that apical and basal inputs interact in non-linear ways. This bias is dependent
507 on the distribution of synaptic inputs along the two trees (*Figure 2D-F*), it follows the
508 preference of basal tree inputs under physiological conditions (*Figure 2D*) and is in line with

509 prior work, whereby apical tree ablation had no impact on somatic orientation preference
510 (*Supplementary Figure 9;* Park et al., 2019). Interestingly, while the above would seem to
511 suggest a minor role for apical inputs in the orientation preference of our model cell (*Figure*
512 *2D*), we found that the orientation tuning of the neuron is greatly affected by sodium
513 conductances in the apical - but not the basal - tree (*Figure 4*). Interestingly, while basal
514 sodium channel conductances are not critically important (*Figure 4C*), AMPA and NMDA
515 conductances are necessary in both dendritic trees for orientation tuning (*Figures 4A&B*). This
516 indicates that depolarizations from the basal tree play a key role in shaping neuronal output,
517 even when basal sodium spikes do not. As such, neuronal output is a synergistic phenomenon
518 mostly between apical sodium spikes and basal depolarizations or sodium spikes. Our
519 simulations suggest that a form of *intra-tree dendritic cooperativity* - a synergistic effect
520 between apical and basal dendritic segments that exhibit activity in relative synchrony - might
521 be present in these neurons. This is supported by the existence of extinction-prone
522 "cooperative" somatic spikes that are lost when either of their dendritic components (apical
523 or basal, be that depolarization or spiking) is lost (*Figure 3*). Additional evidence is provided
524 by the experiments in which removal or suppression (decrease in conductance) of basal
525 stimulus-driven synapses (i.e. only background-driven synapses are fully active) significantly
526 decreases the quality of orientation tuning (i.e. OSI values) in the model neuron, or abolishes
527 tuning altogether (*Figures 4A&B*).

528 A potential explanation for the differential contributions of apical and basal dendrites lies
529 with their morphological and electrophysiological properties. Despite featuring a uniform
530 sodium conductance throughout both dendritic trees, basal dendrites have higher sodium
531 spiking thresholds than apical dendrites with similar electrotonic constant values. Moreover,

532 apical dendrites have highly variable spiking thresholds (*Figure 5D*). This is likely because the
533 soma acts as a current sink, effectively increasing the sodium spiking threshold of all soma-
534 proximal branches (mostly basal dendrites). Meanwhile, the majority of apical dendrites
535 feature much better electrical isolation from the soma due to distance and branching, and
536 are as such exempt from such current sink effects, instead only suffering a loss of current from
537 other connected apical dendritic branches. As such, they exhibit a much greater range of
538 possible thresholds compared to basal dendrites of similar volume (*Figure 5D*), while
539 simultaneously featuring greater signal attenuation (*Supplementary Figure 8C&E*). Put
540 together, these results indicate that apical dendrites overcome their signal attenuation deficit
541 (compared to basal dendrites) by having a greater propensity for dendritic sodium spike
542 generation for different amounts of input. This suggests that sodium spikes are more difficult
543 to induce in basal compared to apical dendrites, offering a potential explanation as to why
544 apical sodium conductances contribute more to somatic output.

545 Taken together, our model predicts that somatic output in L2/3 V1 pyramidal neurons is likely
546 to be determined through *Bimodal Input Coincidence*, a subcategory of coincidence detection
547 (*Abstract Figure*). Specifically, we propose that the basal tree receives visual feedforward
548 input, representing the information therein as a series of hyperpolarizations, depolarizations,
549 and occasional dendritic spikes. Thus, visual input creates a basal "backdrop" of
550 depolarizations that represents visual information. At the same time, predictive and
551 attentional signals from higher-order cortical areas reach the apical tree of the neuron,
552 causing the generation of dendritic spikes that propagate to the soma and are temporally
553 summed with any concurrent basal depolarization. In the event that visual input is non-
554 existent, or of a non-preferred orientation, the depolarization is minimal to none. Thus, the

apical dendritic spike will not be significantly augmented through summation and will fail to produce a somatic response in the majority of cases. If there is visual input, however, especially of an orientation matching the preferred orientation of the basal tree, the aforementioned “backdrop” will include multiple subthreshold depolarizations, perhaps even dendritic spikes. The apical dendritic spikes are thus likely to be temporally summed with these depolarizations and generate a somatic spike. As such, even though most somatic spikes will be generated through an apical tree dendritic spike, the cases in which this is possible in the first place will be dictated by the backdrop of depolarizations (and/or spikes) provided by the basal tree.

The findings presented here propose a more central role for the apical tree than previously suggested. Specifically, in Park et al. (2019), we found that orientation selectivity was not abolished by *in vivo* laser ablation of the apical tree in L2/3 mouse V1 pyramidal neurons, remaining essentially unchanged following a recovery period of ~1 day. Importantly, the model presented here reproduces the *in vivo* ablation findings of the aforementioned study (see Extended Methods, section 8.3.8; *Supplementary Figure 9*). What is seen as a contradiction is resolved by considering that in both Park et al. (2019) and the simulations presented here, apical dendrite ablation is assumed to be accompanied by homeostatic alterations that counteract the increase in input resistance from the loss of the apical tree. These homeostatic mechanisms keep the firing rate of the neuron the same pre- and post-ablation, as seen experimentally (Park et al., 2019). Thus, the contribution of the apical tree to somatic spiking in the intact neuron can be obviated by homeostatic mechanisms following apical tree ablation.

Our findings suggest that L2/3 V1 pyramidal cells may perform salient feature extraction from

visual input compatible with predictive coding (Rao & Ballard, 1999). When top-down signals reflecting attentional or predictive processes reach the apical tree, they “highlight” appropriate parts of the signal “landscape” generated by the visual input reaching the basal trees through the generation of apical dendritic sodium spikes. This could result in a neuron that is activated only when specific features are present in its receptive field, facilitating the processing of salient stimuli. Such phenomena have been observed experimentally as a result of attention (Simons & Chabris, 1999).

However, this work also suffers from a number of limitations. Our findings are inherently bound to the particular characteristics of the simulated morphology. To ensure their generality, further exploration of different neuronal morphologies of L2/3 V1 neurons is required. However, given that our findings correlate with specific anatomical and electrophysiological features of the model neuron (*Figure 5, Supplementary Figure 8*), it would be possible to infer whether the behavior we observe in our model could be present in other neuronal morphologies as well. In addition, while repeating our analysis using other morphologies is beyond the scope of this study (validating model function and performing the extensive parameter exploration reported here is highly resource-intensive), our code and all analysis scripts are made publicly available, allowing interested scientists to apply our approach to other morphologies. The sensitivity analysis that we added in Section 3.4.1 (Supplementary Figure 7) also further establishes the robustness of our findings within biologically relevant ranges of ionic conductances. We have taken all these steps in order to more conclusively demonstrate that our findings are likely to generalize to other L2/3 V1 pyramidal neurons. Furthermore, our model is limited by the lack of data on dendritic features such as signal attenuation and distribution of ion channel conductances. However, this has

been counteracted at least to some extent by the use of experimental data (e.g. see *Supplementary Figure 2*) and the sensitivity analysis, which demonstrates that our conclusions are robust to biologically relevant variations of the key conductances (*Supplementary Figure 7*). Additionally, the single-neuron model sacrifices much of the complexity found in the actual L2/3 network, especially concerning inhibitory inputs, which in our model are not patterned according to different interneuron subtypes and are background-driven, lacking tuning and featuring firing rates lower than stimulus-driven excitatory synapses. A similar complexity loss is incurred by using a relatively simple stimulation protocol, compared to the alternating stimulation of the "drifting gradient" protocol that is more widely used. Finally, the model does not account for retinotopically shifted inhibitory inputs (e.g. Rossi et al., 2020). Retinotopic shift in inhibitory inputs would not affect our results, since stimulation is implicitly assumed to only take place at the center of the receptive field of the model neuron, a fact which would render any retinotopically offset neurons quiescent. Additionally, although inhibitory inputs could be biased towards one dendritic tree over the other, the overall effect of such an imbalance would be a change in the net amount of excitation received by each tree - a scenario which we already explore in part (*Figure 2* and *Figure 3*), finding tuning and somatic spike generation to be generally unaffected. The omission of these features that were unlikely to influence the presence or absence of orientation tuning was performed in an attempt to reduce the complexity (and thus computational requirements) of the model.

In terms of questions that still need to be answered, the exact nature of the attentional and predictive signals received by the apical tree remains to be deciphered. Secondly, the formation of the visual "backdrop" as a result of basal tree depolarization merits further study. Encoding of visual information using mostly subthreshold depolarizations in the

presence of noise is an interesting problem, possibly resolved through the effects of intra-tree dendritic cooperativity, where apical spikes sharpen responses to stimulus-driven input rather than noise, improving the signal-to-noise ratio (Poleg-Polsky, 2019). In addition, a number of differences emerge when comparing the visual system across different model species. In rodents, orientation-selective cells akin to V1 simple cells have been discovered in the thalamus itself (Scholl et al., 2013), and direct thalamocortical projections to L1 of V1 have also been observed (Roth et al., 2016). Furthermore, rodent V1 organization follows a dispersed salt-and-pepper motif, unlike the highly structured organization typical of higher mammals like primates and cats (Ohki & Reid, 2007). These differences are important to take into account when trying to infer general rules of function from information derived from rules of information processing in different animal models. Finally, perhaps the most interesting unanswered question is whether these computations take place elsewhere in the cortex in addition to the visual system. Predictive coding as a means of stimulus compression has already been proposed as a way to simplify visual perception (Rao & Ballard, 1999), and this might also be the case for other sensory or cognitive tasks. Regardless, further investigation is required in order to unravel the Gordian knot that is visual perception.

5. Acknowledgments

This work was supported by the ERC Starting Grant “dEMORY: Dissecting the role of dendrites in memory”, ERC-2012-StG-311435, the Fondation Santé, a FORTH-Synergy Grant (EVO-NMDA) and the NEUREKA grant H2020-FETOPEN-2018- 2019-2020-01 to YP, the NIH NEI R01 grant EY-024019 and NINDS R21 grant NS088457 to SS, a Hellenic Foundation for Research and Innovation (HFRI) PhD Scholarship (no. 6731) to K-E.P, and the FORTH-Synergy Grant

(FlexBe) to AP.

6. References

1. Adesnik, H., Bruns, W., Taniguchi, H., Huang, Z. J., & Scanziani, M. (2012). A neural circuit for spatial summation in visual cortex. *Nature*, *490*(7419), 226–231. https://doi.org/10.1038/nature11526
2. Behabadi, B. F., Polsky, A., Jadi, M., Schiller, J., & Mel, B. W. (2012). Location-dependent excitatory synaptic interactions in pyramidal neuron dendrites. *PLoS Computational Biology*, *8*(7), 40–42. https://doi.org/10.1371/journal.pcbi.1002599
3. Chen, T.-W., Wardill, T. J., Sun, Y., Pulver, S. R., Renninger, S. L., Baohan, A., Schreiter, E. R., Kerr, R. A., Orger, M. B., Jayaraman, V., Looger, L. L., Svoboda, K., & Kim, D. S. (2013). Ultrasensitive fluorescent proteins for imaging neuronal activity. *Nature*, *499*(7458), 295–300. https://doi.org/10.1038/nature12354
4. Cho, K.-H., Jang, H.-J., Lee, E.-H., Yoon, S. H., Hahn, S. J., Jo, Y.-H., Kim, M.-S., & Rhie, D.-J. (2008). Differential Cholinergic Modulation of Ca2+ Transients Evoked by Backpropagating Action Potentials in Apical and Basal Dendrites of Cortical Pyramidal Neurons. *Journal of Neurophysiology*, *99*(6), 2833–2843. https://doi.org/10.1152/jn.00063.2008
5. Coogan, T. A., & Burkhalter, A. (1990). Conserved patterns of cortico-cortical connections define areal hierarchy in rat visual cortex. *Experimental Brain Research*, *80*(1), 49–53. https://doi.org/10.1007/BF00228846
6. Cruz-Martín, A., El-Danaf, R. N., Osakada, F., Sriram, B., Dhande, O. S., Nguyen, P. L., Callaway, E. M., Ghosh, A., & Huberman, A. D. (2014). A dedicated circuit links direction-selective retinal ganglion cells to the primary visual cortex. *Nature*, *507*(7492), 358–361. https://doi.org/10.1038/nature12989
7. Defelipe, J., Elston, G. N., Fujita, I., Fuster, J., Harrison, K. H., Hof, P. R., Kawaguchi, Y., Martin, K. A. C., Rockland, K. S., Thomson, A. M., Wang, S. S. H., White, E. L., & Yuste, R. (2002). Neocortical circuits: Evolutionary aspects and specificity versus non-specificity of synaptic connections. Remarks, main conclusions and general comments and discussion. *Journal of Neurocytology*, *31*(3-5 SPEC. ISS.), 387–416. https://doi.org/10.1023/A:1024142513991
8. DeFelipe, J., & Fariñas, I. (1992). The pyramidal neuron of the cerebral cortex: morphological and chemical characteristics of the synaptic inputs. *Prog Neurobiol*, *39*(6), 563–607. https://doi.org/10.1016/0301-0082(92)90015-7
9. Goetz, L., Roth, A., & Häusser, M. (2021). Active dendrites enable strong but sparse inputs to determine orientation selectivity. *Proceedings of the National Academy of Sciences of the United States of America*, *118*(30). https://doi.org/10.1073/pnas.2017339118
10. Haider, B., Häusser, M., & Carandini, M. (2013). Inhibition dominates sensory responses in the awake cortex. *Nature*, *493*(7430), 97–100. https://doi.org/10.1038/nature11665
11. Hines, M. L., & Carnevale, N. T. (2001). Neuron: A Tool for Neuroscientists. *The Neuroscientist*, *7*(2), 123–135. https://doi.org/10.1177/107385840100700207
12. Iacaruso, M. F., Gasler, I. T., & Hofer, S. B. (2017). Synaptic organization of visual space in primary visual cortex. *Nature*. https://doi.org/10.1038/nature23019
13. Jia, H., Rochefort, N. L., Chen, X., & Konnerth, A. (2010). Dendritic organization of

sensory input to cortical neurons in vivo. *Nature*, *16*(3), 236–237. https://doi.org/10.1038/nature08947

14. Ju, N., Li, Y., Liu, F., Jiang, H., Macknik, S. L., Martinez-Conde, S., & Tang, S. (2020). Spatiotemporal functional organization of excitatory synaptic inputs onto macaque V1 neurons. *Nature Communications*, *11*(1). https://doi.org/10.1038/s41467-020-14501-y
15. Keller, A. J., Roth, M. M., & Scanziani, M. (2020). Feedback generates a second receptive field in neurons of the visual cortex. *Nature*, *582*(7813), 545–549. https://doi.org/10.1038/s41586-020-2319-4
16. Ko, H., Hofer, S. B., Pichler, B., Buchanan, K. A., Sjöström, P. J., & Mrsic-Flogel, T. D. (2011). Functional specificity of local synaptic connections in neocortical networks. *Nature*, *473*(7345), 87–91. https://doi.org/10.1038/nature09880
17. Larkum, M. (2013). A cellular mechanism for cortical associations: An organizing principle for the cerebral cortex. *Trends in Neurosciences*, *36*(3), 141–151. https://doi.org/10.1016/j.tins.2012.11.006
18. Mrsic-Flogel, T. D., Hofer, S. B., Ohki, K., Reid, R. C., Bonhoeffer, T., & Hübener, M. (2007). Homeostatic Regulation of Eye-Specific Responses in Visual Cortex during Ocular Dominance Plasticity. *Neuron*, *54*(6), 961–972. https://doi.org/10.1016/j.neuron.2007.05.028
19. Ohki, K., & Reid, R. C. (2007). Specificity and randomness in the visual cortex. *Current Opinion in Neurobiology*, *17*(4), 401–407. https://doi.org/10.1016/j.conb.2007.07.007
20. Pachitariu, M., Stringer, C., Dipoppa, M., Schröder, S., Rossi, L. F., Dalgleish, H., Carandini, M., & Harris, K. (2016). Suite2p: beyond 10,000 neurons with standard two-photon microscopy. *BioRxiv*, *July*, 061507. https://doi.org/10.1101/061507
21. Palmer, L. M., Shai, A. S., Reeve, J. E., Anderson, H. L., Paulsen, O., & Larkum, M. E. (2014). NMDA spikes enhance action potential generation during sensory input. *Nature Neuroscience*, *17*(3), 383–390. https://doi.org/10.1038/nn.3646
22. Papadopoulos, P. M., Katz, M. J., & Bruno, G. (2003). NPACI rocks: Tools and techniques for easily deploying manageable linux clusters. *Concurrency and Computation: Practice and Experience*, *15*(7–8), 707–725. https://doi.org/10.1002/cpe.722
23. Park, J., Papoutsi, A., Ash, R. T., Marin, M. A., Poirazi, P., & Smirnakis, S. M. (2019). Contribution of apical and basal dendrites to orientation encoding in mouse V1 L2/3 pyramidal neurons. *Nature Communications*, *10*(1), 1–11. https://doi.org/10.1038/s41467-019-13029-0
24. Poleg-Polsky, A. (2019). Dendritic spikes expand the range of well tolerated population noise structures. *Journal of Neuroscience*, *39*(46), 9173–9184. https://doi.org/10.1523/JNEUROSCI.0638-19.2019
25. Rao, R. P. N., & Ballard, D. H. (1999). Predictive coding in the visual cortex: A functional interpretation of some extra-classical receptive-field effects. *Nature Neuroscience*, *2*(1), 79–87. https://doi.org/10.1038/4580
26. Rossi, L. F., Harris, K. D., & Carandini, M. (2020). Spatial connectivity matches direction selectivity in visual cortex. *Nature*, *588*(7839), 648–652. https://doi.org/10.1038/s41586-020-2894-4
27. Roth, M. M., Dahmen, J. C., Muir, D. R., Imhof, F., Martini, F. J., & Hofer, S. B. (2015). Thalamic nuclei convey diverse contextual information to layer 1 of visual cortex.

Nature Neuroscience, *19*(2), 299–307. https://doi.org/10.1038/nn.4197

28. Roth, M. M., Dahmen, J. C., Muir, D. R., Imhof, F., Martini, F. J., & Hofer, S. B. (2016). Thalamic nuclei convey diverse contextual information to layer 1 of visual cortex. *Nature Neuroscience*, *19*(2), 299–307. https://doi.org/10.1038/nn.4197
29. Schindelin, J., Arganda-Carreras, I., Frise, E., Kaynig, V., Longair, M., Pietzsch, T., Preibisch, S., Rueden, C., Saalfeld, S., Schmid, B., Tinevez, J. Y., White, D. J., Hartenstein, V., Eliceiri, K., Tomancak, P., & Cardona, A. (2012). Fiji: An open-source platform for biological-image analysis. *Nature Methods*, *9*(7), 676–682. https://doi.org/10.1038/nmeth.2019
30. Scholl, B., Tan, A. Y. Y., Corey, J., & Priebe, N. J. (2013). Emergence of Orientation Selectivity in the Mammalian Visual Pathway. *Journal of Neuroscience*, *33*(26), 10616–10624. https://doi.org/10.1523/JNEUROSCI.0404-13.2013
31. Schuz, A., & Palm, G. (1989). Density of Neurons and Synapses. *Journal of Comparative Neurology*, *455*, 442–455.
32. Simons, D. J., & Chabris, C. F. (1999). Gorillas in our midst: sustained inattentional blindness for dynamic events. *Perception*, *28*(28), 1059–1074.
33. Smith, S. L., Smith, I. T., Branco, T., & Häusser, M. (2013). Dendritic spikes enhance stimulus selectivity in cortical neurons in vivo. *Nature*, *503*(7474), 115–120. https://doi.org/10.1038/nature12600
34. Spruston, N. (2008). Pyramidal neurons: dendritic structure and synaptic integration. *Nature Reviews Neuroscience*, *9*(3), 206–221. https://doi.org/10.1038/nrn2286
35. van Elburg, R. A. J., & van Ooyen, A. (2010). Impact of dendritic size and dendritic topology on burst firing in pyramidal cells. *PLoS Computational Biology*, *6*(5), 1–19. https://doi.org/10.1371/journal.pcbi.1000781
36. Wilson, D. E., Whitney, D. E., Scholl, B., & Fitzpatrick, D. (2016). Orientation selectivity and the functional clustering of synaptic inputs in primary visual cortex. *Nature Neuroscience*, *19*(8), 1003–1009. https://doi.org/10.1038/nn.4323

7. Supplementary Information

Compartment Type	Passive/Active Mechanisms	Synaptic Mechanisms
Soma	Hodgkin/Huxley voltage-gated Na^+ channels Hodgkin/Huxley voltage-gated K^+ channels Muscarinic voltage-gated K^+ channels A-Type voltage-gated K^+ channels T-Type Ca^{++} channels High voltage activated (HVA) Ca^{++} channels Calcium-dependent K^+ channels Active ATP Ca^{++} pumps	$GABA_A$ (background-driven)
Basal Dendrites		AMPA (background-driven) NMDA (background-driven) $GABA_A$ (background-driven) AMPA (stimulus-driven) NMDA (stimulus-driven) $GABA_A$ (stimulus-driven)
Apical Dendrites		

***Supplementary Table 1**. Outline of passive, active and synaptic mechanisms present in the model neuron.*

Conductance (mS/cm^2)	Soma	Apical	Basal
g_{Na}	0.505	0.303	0.303
g_{Kdr}	0.05	$1.5*10^{-3}$	$1.5*10^{-3}$
g_{Km}	$2.8*10^{-3}$	$1.27*10^{-3}$	$1.27*10^{-3}$
g_A	5.4	Diameter ≤ 0.8 µm: 108 Diameter > 0.8 µm: 10.8	Diameter ≤ 0.8 µm: 108 Diameter > 0.8 µm: 10.8
g_T	0.03	x ≤ 260 µm: 0.029*sin(0.009*x+0.88) x > 260µm: 0.012	$0.03+6*10^{-5}*x$
g_{HVA}	$0.05*10^{-3}$	x ≤ 260 µm: $0.049*10^{-3}*\sin(0.009*x+0.88)$ x > 260µm: $0.02*10^{-3}$	$0.05*10^{-3}+10^{-7}*x$
g_{KCa}	$2.1*10^{-3}$	$2.1*10^{-3}$	$2.1*10^{-3}$

***Supplementary Table 2**. Outline of membrane mechanism conductances (not synaptic). Reproduced from* (Park et al., 2019).

	Model	Cho et al., 2010
RMP, mV	-79	-78.56 ± 1.34
IR, MΩ	123.6	125.2 ± 8.2
τ, ms	17.3	16 ± 0.7
AP amplitude, mV	66.1	67.8 ± 1.8
AP threshold, mV	-41.8	-37.7 ± 1.3
AHP, mV	17.9	13.3 ± 0.5
P-T time, ms	38.6	55.3 ± 2.7
AP adaptation	1.16	1.18 ± 0.02

***Supplementary Table 3**. Outline of model electrophysiological properties. RMP: resting membrane potential, IR: Input Resistance measured at hyperpolarizing current (-0.04 nA), AP: action potential, AHP: after hyperpolarization measured at depolarizing current (0.16 nA), P-T peak-trough. Reproduced from* (Park et al., 2019).

	Conductance (nS)	**τ_1, ms**	**τ_2, ms**
NMDA	1.15	2	30
AMPA	0.84	0.1	2.5
$GABA_A$	1.25	0.2	1.4

***Supplementary Table 4.** Outline of synaptic mechanism conductances and time constants. Reproduced from* (Park et al., 2019).

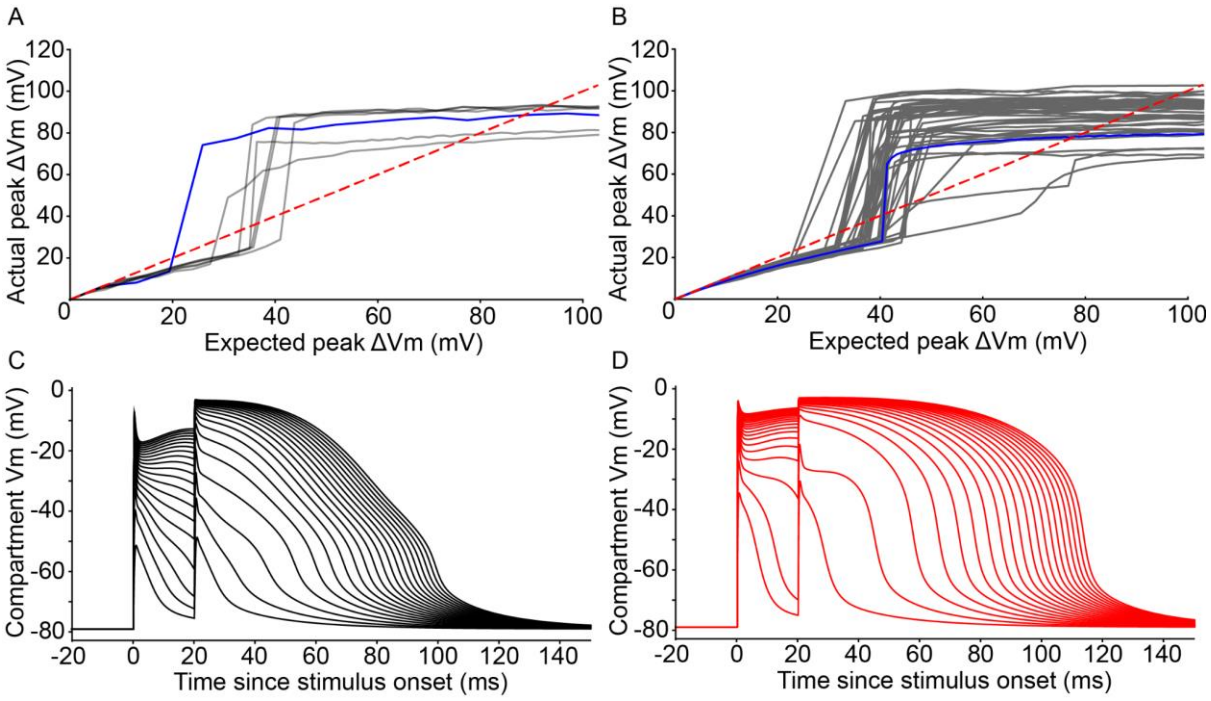

***Supplementary Figure 1.** Visualization of dendritic non-linear properties. A: Expected vs Actual plot for all basal dendrites undergoing the I3P protocol for 1-200 synapses. Blue line represents the dendrite in Figure 1B (basal dendrite #0). B: Same as A, but for all apical dendrites. Blue line represents dendrite in Figure 1C (apical dendrite #0). C: Example traces from the I3P protocol for NMDA spike generation from basal dendrite #0. Traces are 10*

synapses apart from each other. D: Same as C, but for apical dendrite #42 (oblique branch). Dendrites in C and D chosen to show examples of NMDA spiking.

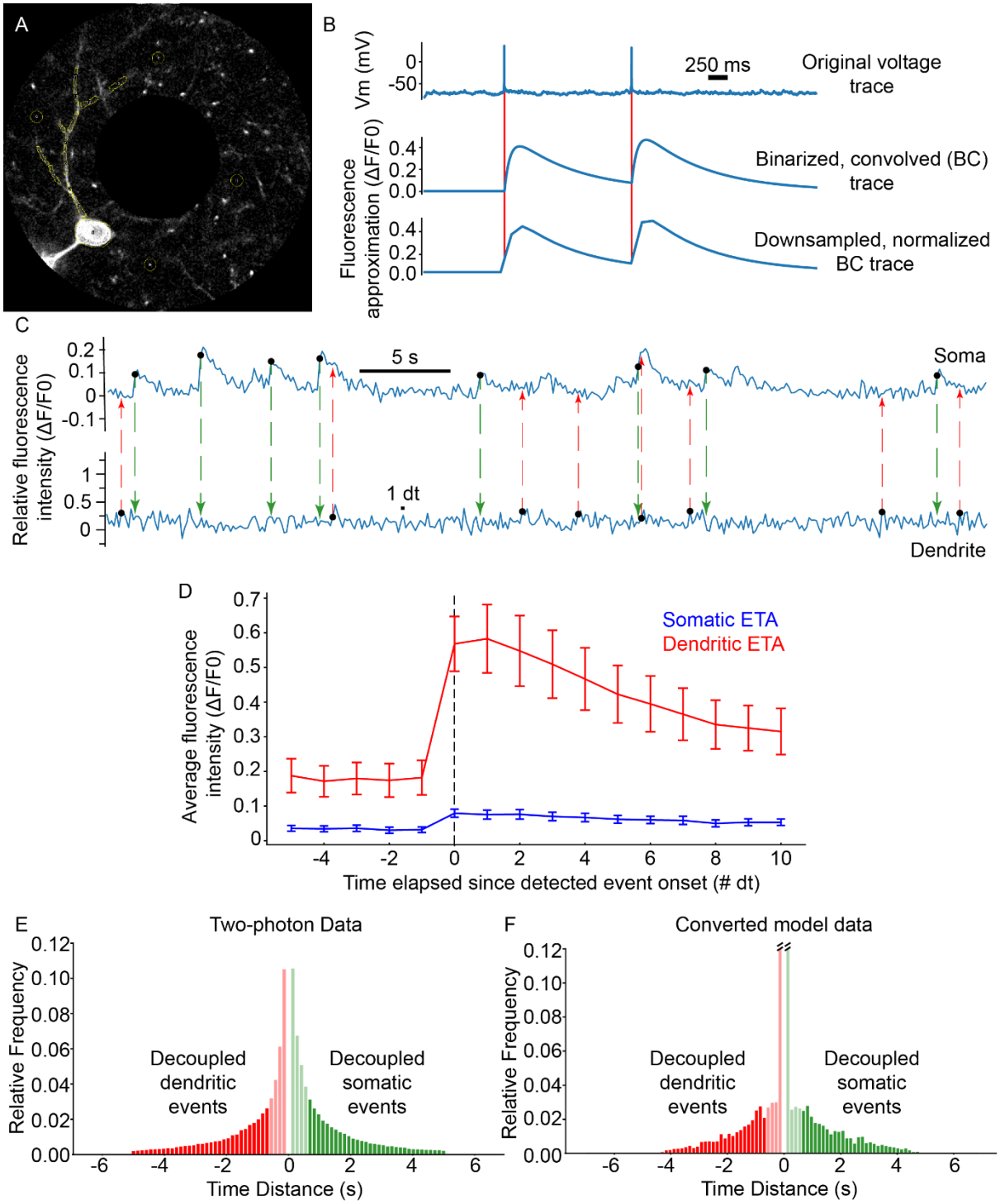

Supplementary Figure 2. Comparing Model Output with Two-Photon Imaging Data*. Simultaneous recordings from basal dendritic segments and somata of L2/3 V1 pyramidal neurons were performed in anesthetized mice (spontaneous activity of 11 neurons from 2 mice, see Extended Methods, section 8.5; panel A). These imaging*

data were compared to modeling data generated using the spontaneous activity protocol, whereby simulations feature only background activity, i.e. noise, in the absence of a visual stimulus (see Extended Methods, section 8.3.5). A: Image from one of the neurons in the dataset. Note the separate, multiple ROIs per dendritic segment, as well as the 4 circular ROIs used for background fluorescence calculation. B: Example traces from the model data conversion pipeline. Voltage spiking data is binarized and convolved with a GcaMP6s kernel function (Supplementary Figure 3). Resulting data is downsampled to two-photon sampling rates (~7.25 Hz) from the original sampling rate (10 KHz), and processed exactly like in vivo *two-photon fluorescence data. Red vertical lines show the timing of the original spikes. C: Example somatic (top) and distal dendritic (bottom)* $\Delta F/F_0$ *traces from the neuron in (A). Black dots at the origin of colored dashed lines denote detected events. Note that somatic events (green dashed lines/arrows) are not necessarily coincident with dendritic events (red dashed lines/arrows). D: Event-triggered averages for all somatic (blue) and basal dendritic segment ROIs (1 dt* $\simeq$ *0.138 s; error bars: Standard error of the mean). E: Event pair timing difference histogram for the two-photon data. 48.12% of event pairs feature basal dendritic events that are decoupled from the soma (red; dendritic events occur at least 1 dt before the onset of a somatic spike), with 27.8% being decoupled if the 4 bins (~552 ms) closest to zero are excluded (excluded data marked as lightly shaded bars). F: Event pair timing difference histogram for the converted model data. 48.79% of event pairs feature basal dendritic events that are decoupled from the soma (red; dendritic events occur at least 1 dt before the onset of a somatic spike), with 24.3% being decoupled if the 4 bins (~552 ms) closest to zero are excluded (excluded data marked as lightly shaded bars). Note that in both D and E, the zero-difference bin was removed, as it is assumed to contain the majority of backpropagating events. The middle two bars in F have been truncated for visualization purposes; the corresponding values are (left to right) 0.15958 and 0.16533, respectively. Some of the detected somatic events are not closely preceded by any detected basal dendritic events (panel F, green bars), suggesting that other events, perhaps arising in the apical tree or basal dendritic segments not in the recording field of view, contribute to somatic activity in such cases.*

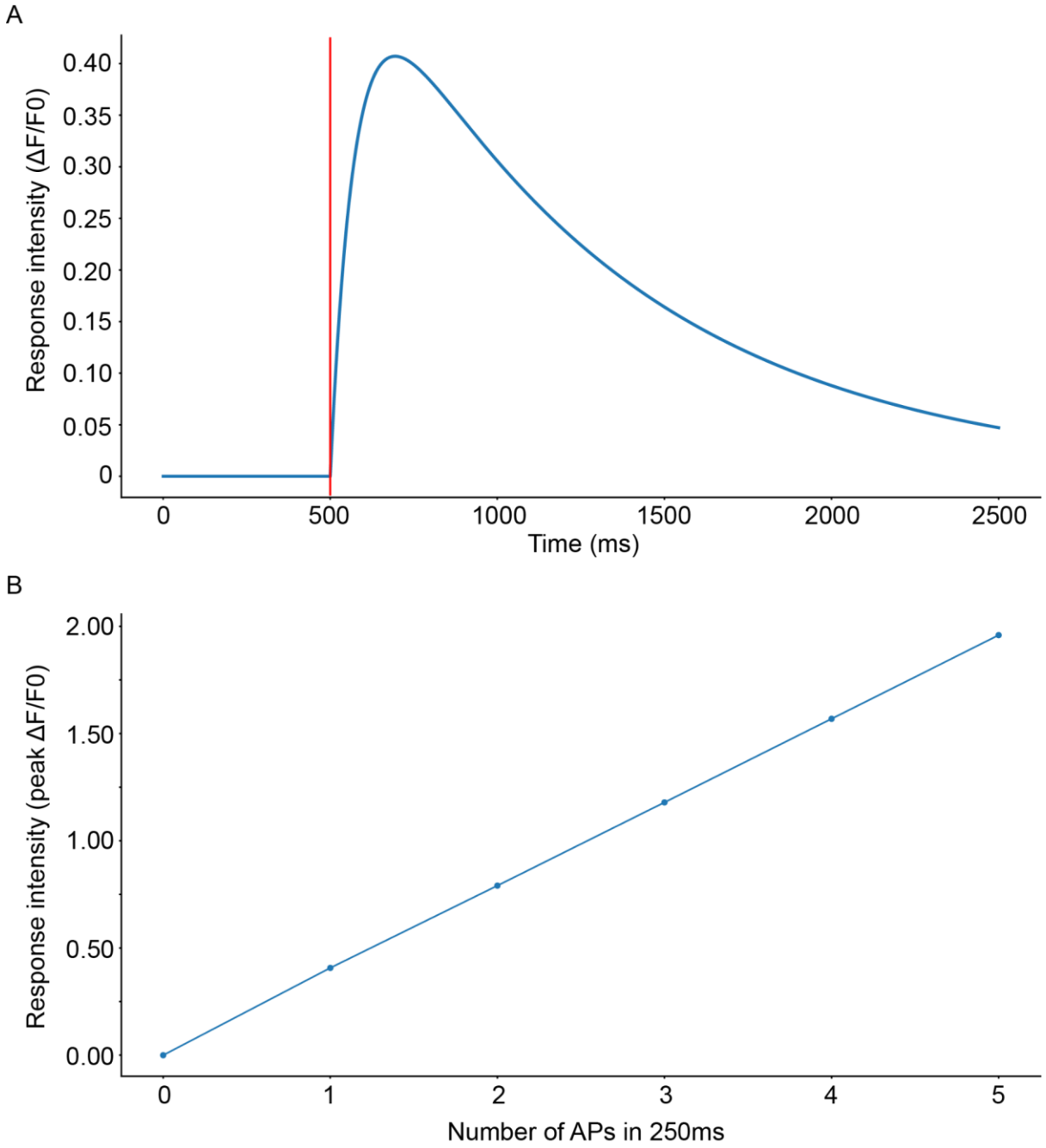

833

834 ***Supplementary Figure 3.*** *Properties of the GcaMP6s kernel. A: Illustration of the output of the kernel function*

835 *for a single event (AP) occurring at* t_0 *= 500 ms. (marked as a red line). B: Response intensity as a function of the*

836 *number of events (APs) within a 250ms window. Compare with* (Chen et al., 2013).

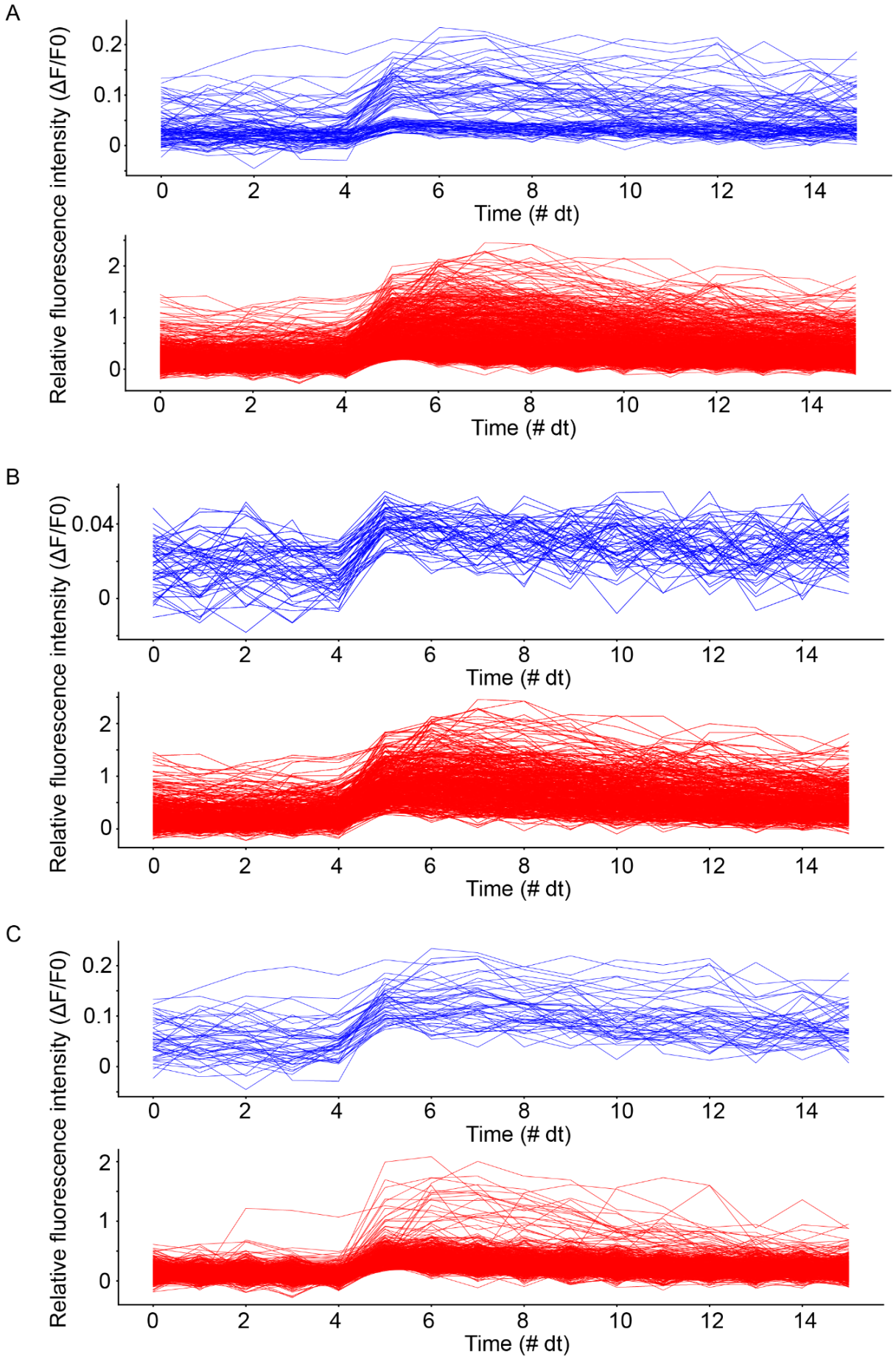
A
Relative fluorescence intensity (ΔF/F0)
0.2
0.1
0
0
2
4
6
8
10
12
14
Time (# dt)
2
1
0
Time (# dt)
B
Relative fluorescence intensity (ΔF/F0)
0.04
0
Time (# dt)
2
1
0
Time (# dt)
C
Relative fluorescence intensity (ΔF/F0)
0.2
0.1
0
Time (# dt)
2
1
0
Time (# dt)

837

Supplementary Figure 4. *Waveforms of detected calcium fluorescence events. Somatic waveforms in blue, basal dendritic waveforms in red. Spike onset detected at t = 5 dt. A: Waveforms from all detected events from both mice. B: Waveforms from all detected events in mouse 1. C: Waveforms from all detected events from mouse 2. Note: 1 dt is equal to approximately 0.138 s, and exactly equal to the microscope recording frame time.*

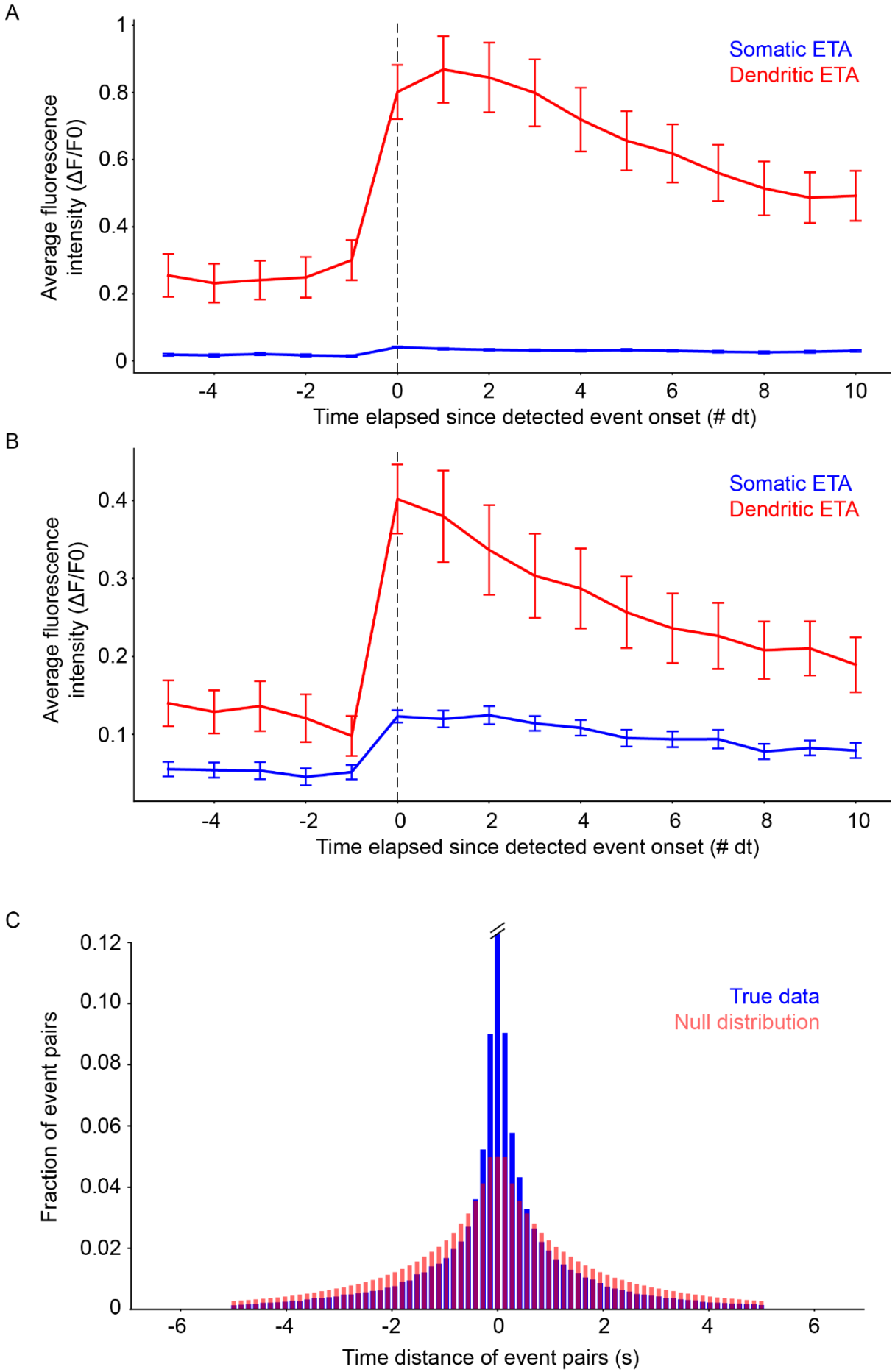
A
Average fluorescence intensity (ΔF/F0)
Somatic ETA
Dendritic ETA
Time elapsed since detected event onset (# dt)
B
Average fluorescence intensity (ΔF/F0)
Somatic ETA
Dendritic ETA
Time elapsed since detected event onset (# dt)
C
Fraction of event pairs
True data
Null distribution
Time distance of event pairs (s)

843

Supplementary Figure 5. *A: Event-triggered averages for somatic (blue) and basal dendrite (red) events in mouse 1. B: Event-triggered averages for somatic (blue) and basal dendrite (red) events in mouse 2. Note the difference in fluorescence intensity compared to mouse 1. Error bars: Standard error of the mean. C: Comparison of the true (two-photon) data distribution (blue) with the null distribution (light red). Distributions are different (K.S. two-sample test; test value ~0.105, $p << 0.05$). Note that the middle bar for the true data has been truncated (actual value 0.12267).*

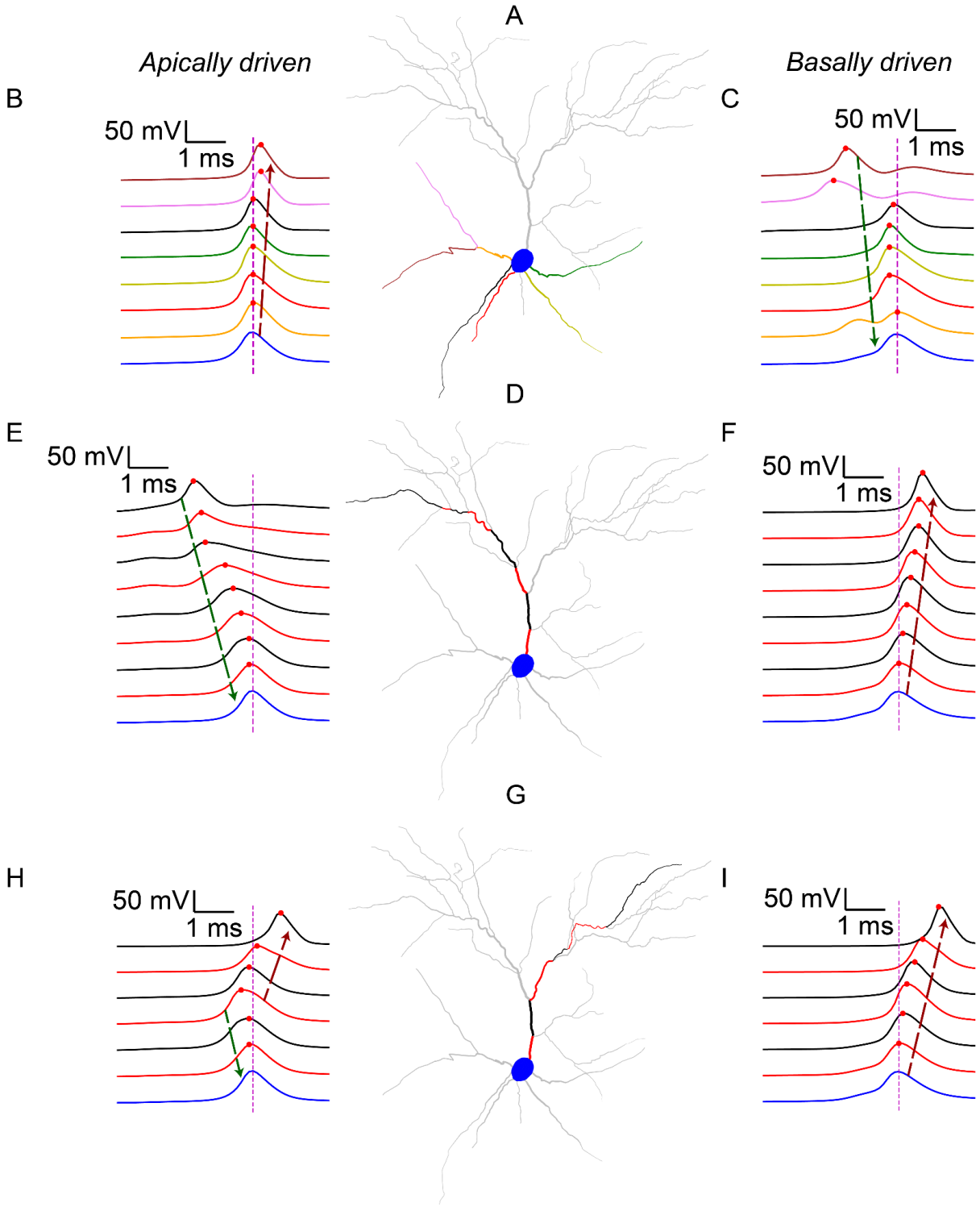

Supplementary Figure 6. *Example traces showing the spatiotemporal evolution of somatodendritic voltage before, during and after the generation of a dendritic-sodium-mediated somatic spike, across different dendritic paths. A: Visualization of basal dendrites. Colors correspond to traces in panels B and C. B: Voltage traces from the basal dendrites and soma (blue) around the occurrence of an apically-driven somatic spike. C: Voltage traces from the basal dendrites and soma (blue) around the occurrence of a basally-driven somatic spike. D:*

Visualization of a specific apical path. Colors correspond, in the same sequence (proximal to distal), to the traces in panels E and F. E: Voltage traces from the soma (blue) and the apical dendritic segments shown in D around the occurrence of an apically-driven somatic spike. F: Voltage traces from the soma (blue) and the apical dendritic segments shown in D around the occurrence of a basally-driven somatic spike. G: As in D, but for a different apical path. H: As in E, but for a different apical path. I: As in F, but for a different apical path. In all panels, traces are ordered by distance of the recording point from the soma (closest to farthest). Red dots denote the maximum voltage attained by the corresponding dendritic segment. Magenta dashed line indicates the timing of the somatic spike. The soma (and corresponding somatic trace) is always marked in blue. Dendritic segments colored grey are not inactive during these events, but their activity is not shown directly in these traces. Dashed arrows indicate propagation of potential towards (dark green) or away from (dark red) the soma.

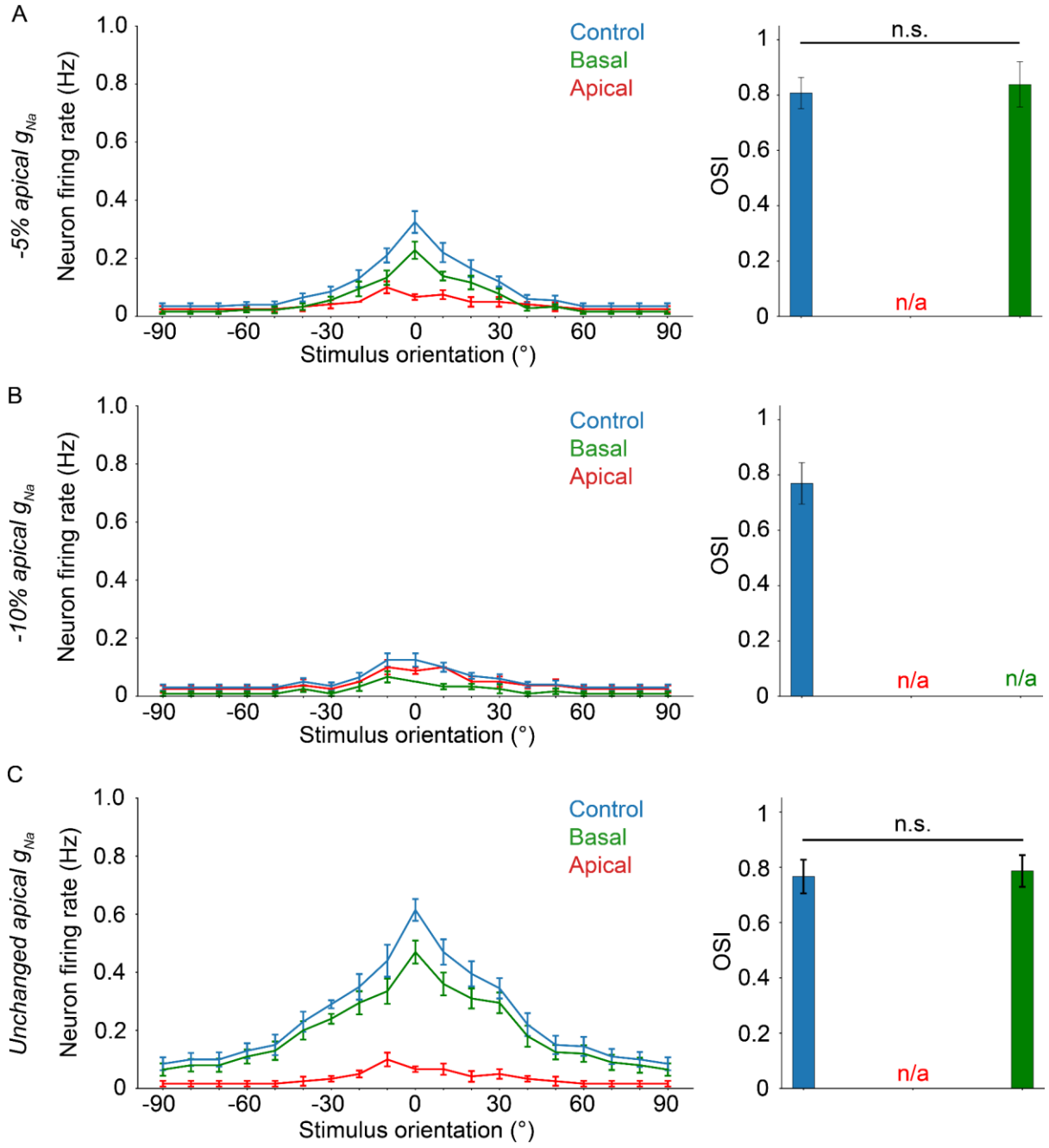

Supplementary Figure 7. *Results from experiments similar to Figure 4C, only with a reduction in apical sodium conductance. A. Apical g_{Na} decreased by 5%. Elimination of the apical sodium component results in total loss of tuning. B. Apical g_{Na} decreased by 10%. Unlike A, elimination of the apical or basal sodium component results in total loss of tuning. C. Apical g_{Na} is unchanged (control condition, identical to Figure 4C). Similar to A, elimination of the apical sodium component results in total loss of tuning. If present, "n/a" denotes a lack of orientation tuning for that specific experimental setup. Stars denote statistical significance at a significance level (α) of 0.05 (*), 0.01 (**) or 0.001 (***), whereas "n.s." stands for "no statistically significant difference", i.e. p-value ≥ α. Dependent two-sample t-tests were used in all cases.*

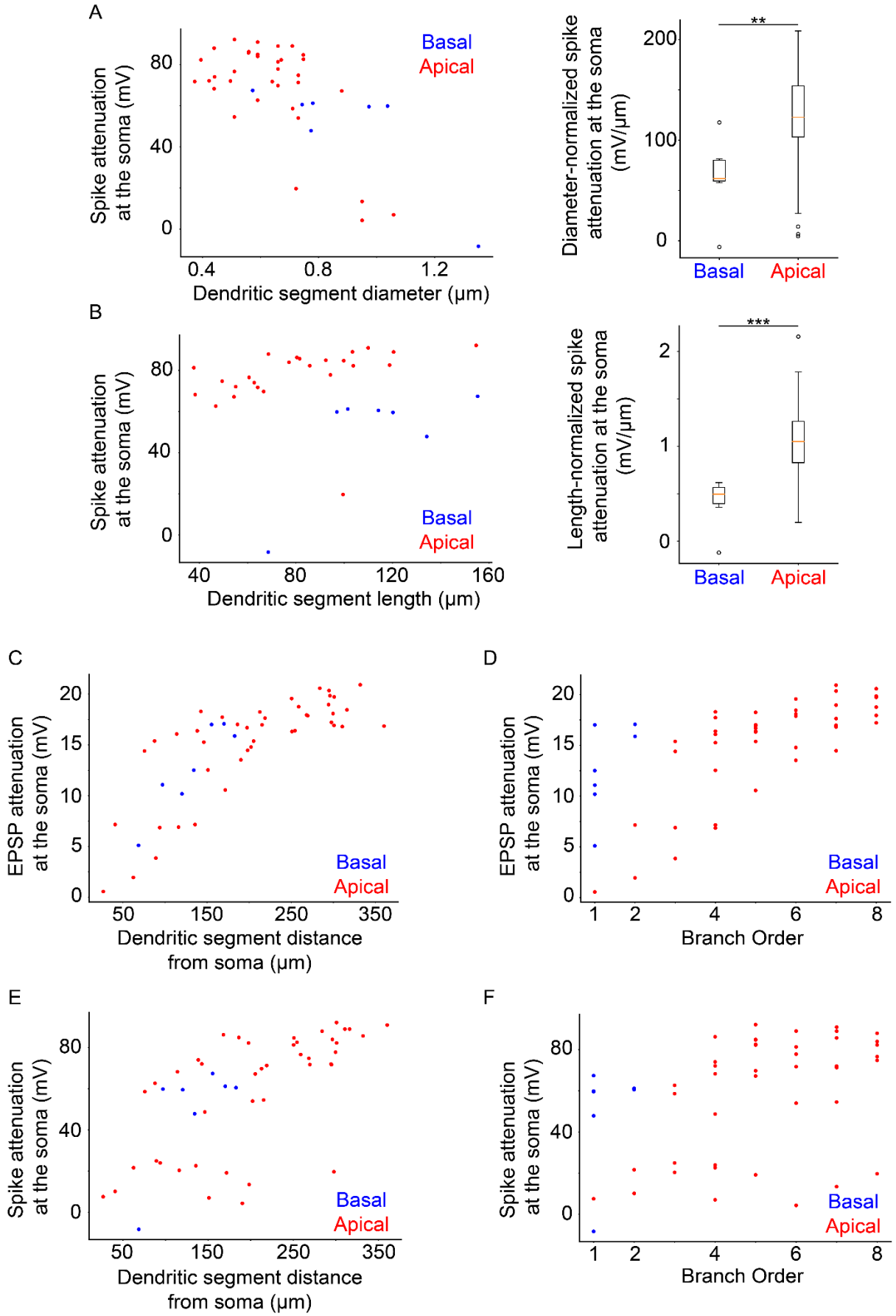
A
Spike attenuation at the soma (mV)
80
40
0
0.4
0.8
1.2
Dendritic segment diameter (μm)
Basal
Apical
Diameter-normalized spike attenuation at the soma (mV/μm)
200
100
0
**
Basal
Apical
B
Spike attenuation at the soma (mV)
80
40
0
40
80
120
160
Dendritic segment length (μm)
Basal
Apical
Length-normalized spike attenuation at the soma (mV/μm)
2
1
0
***
Basal
Apical
C
EPSP attenuation at the soma (mV)
20
15
10
5
0
50
150
250
350
Dendritic segment distance from soma (μm)
Basal
Apical
D
EPSP attenuation at the soma (mV)
20
15
10
5
0
1
2
4
6
8
Branch Order
Basal
Apical
E
Spike attenuation at the soma (mV)
80
40
0
50
150
250
350
Dendritic segment distance from soma (μm)
Basal
Apical
F
Spike attenuation at the soma (mV)
80
40
0
1
2
4
6
8
Branch Order
Basal
Apical

876

877 ***Supplementary Figure 8.*** *Results from analyses similar to Figure 5. Dendritic segments were stimulated with a*
878 *number of synapses sufficient to elicit dendritic sodium spiking, and the attenuation at the soma was measured.*
879 *A: Somatic sodium spike attenuation as a function of dendritic segment diameter (left panel). Differences*
880 *between apical and basal dendrites can be evaluated by normalizing spike attenuation by the diameter of the*
881 *dendritic segment (right panel), showing significantly greater attenuation per µm for apical over basal dendrites*
882 *(p-value 0.006459). B: Somatic sodium spike attenuation as a function of dendritic segment length (left panel).*
883 *Differences between apical and basal dendrites can be evaluated by normalizing spike attenuation by the length*
884 *of the dendritic segment (right panel), showing significantly greater attenuation per µm for apical over basal*
885 *dendrites (p-value 0.000097). C: 20 mV EPSP attenuation as a function of distance of the dendritic segment from*
886 *the soma. D: 20 mV EPSP attenuation as a function of the branch order of the dendritic segment. E: As C, but for*
887 *sodium spikes rather than 20 mV EPSPs. F: As D, but for sodium spikes rather than 20 mV EPSPs. Stars denote*
888 *statistical significance at a significance level (α) of 0.05 (*), 0.01 (**) or 0.001 (***), whereas "n.s." stands for*
889 *"no statistically significant difference", i.e. p-value ≥ α.*

890

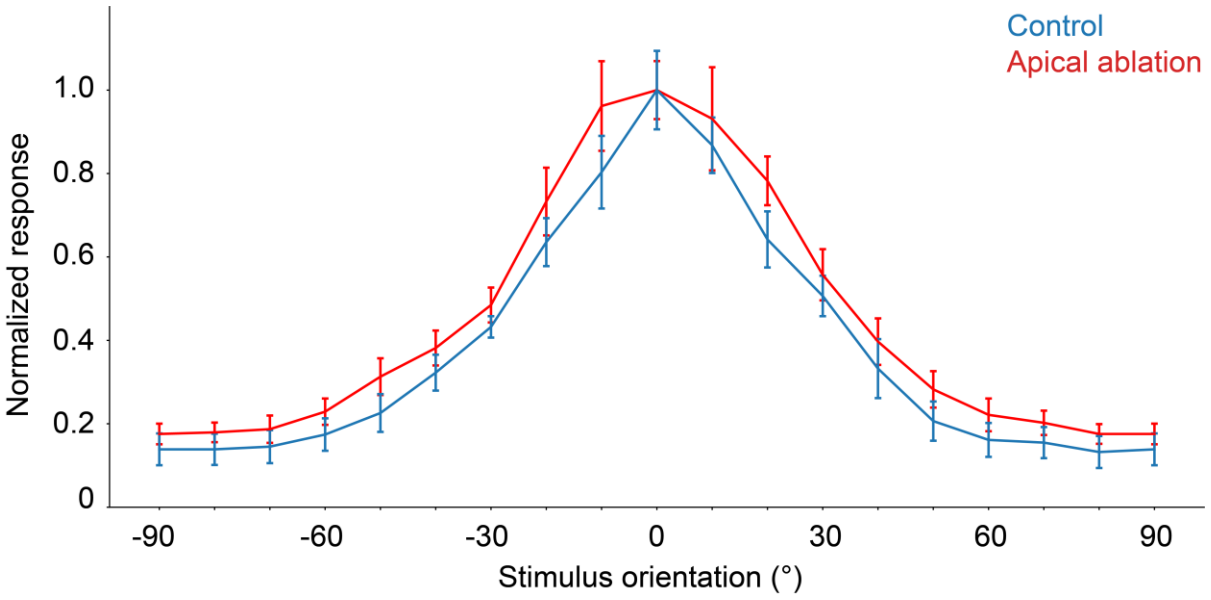

891

892 ***Supplementary Figure 9.*** *Comparison of orientation tuning behavior seen in the model under control (blue) and*
893 *apical dendrite ablation (red) configurations. Note that the y-axis shows the normalized response (firing rate*
894 *values divided by their corresponding maximum). Error bars: standard error of the mean.*

8. Extended Methods

8.1. Model Description

The single neuron model was derived from the L2/3 V1 pyramidal cell model of (Park et al., 2019) created in the NEURON simulation environment (Hines & Carnevale, 2001). It is a morphologically detailed reconstruction, featuring 43 apical dendritic segments, 7 basal dendritic segments and an axon. As the model makes use of a variety of passive and active mechanisms (*Supplementary Tables 1-4*), its electrophysiological properties were validated against experimental data (Park et al., 2019). Neither the morphology nor the biophysical properties of the source model were altered, barring specific ion channel or synaptic changes where explicitly specified.

The model features both excitatory and inhibitory synaptic input. Excitatory input was subdivided into background-driven (noise) and stimulus-driven, the latter consisting of orientation-tuned synapses. Inhibitory synapses are modeled as background-driven (inhibitory noise) which alongside background-driven excitatory synapses (excitatory noise) comprise the background-driven inputs. Stimulus-driven and background-driven synaptic input to the neuron is distributed uniformly on the target compartments using a density of 2 synapses per µm (DeFelipe & Fariñas, 1992; Schuz & Palm, 1989). Activation of synapses occurs via pseudo-randomly generated Poisson spike trains. Background-driven and stimulus-driven synapses feature different peak Poisson activation frequencies (0.11 Hz and 0.3 Hz, respectively) to produce the electrophysiologically-recorded firing rates (Adesnik et al., 2012; Park et al., 2019). Stimulus-driven synapses feature variable activation frequencies, with a maximum of 0.3 Hz, based on the angular distance of the stimulus from the preferred orientation of each individual synapse. Unlike the original model by (Park et al., 2019), apical

stimulus-driven synaptic inputs have had a 10 ms delay added, to better reflect experimental data on feedback synaptic inputs in V1 (Ju et al., 2020).

We modulate the proportion of stimulus-driven excitatory synapses on the apical versus the basal tree in various experiments in order to examine the effects of synaptic input distribution on somatic output. In all cases, the amount of inhibition at the soma is 7% of the total inhibitory synapses (Defelipe et al., 2002). The default synapse distribution was 40% apical to 60% basal ("biologically plausible model"), in adherence with experimental data (excitation: 40% apical, 60% basal; inhibition: 33% apical, 60% basal, 7% soma) (Defelipe et al., 2002). The "inverse biologically plausible" model, conversely, features a 60% apical to 40% basal distribution (excitation: 60% apical, 40% basal; inhibition: 55.8% apical, 37.2% basal, 7% soma). The "even" model features a balanced distribution of synaptic input across both trees (even: excitation: 50% apical, 50% basal; inhibition: 46.5% apical, 46.5% basal, 7% soma). The synaptic distribution of the "even" and "inverse biologically relevant" models are not derived by experimental data, yet they allow for the investigation of apical and basal tree interactions under conditions of balanced or imbalanced synaptic input. We also make use of other distributions biased in either the apical or basal direction (referring to stimulus-driven excitatory input; from 10% basal – 90% apical to 90% basal – 10% apical, in steps of 10%). Similar to above, background-driven synapses closely follow the stimulus-driven synapse distribution in these cases, except for background inhibition, which always features 7% allocated to the soma.

In our model, orientation preference was assigned on two levels: synaptic (input/single synapse) and dendritic (whole tree). Single synapse orientation preference is modeled as a synaptic weight vector biased towards a predefined (preferred) orientation, which also

factors into the activation frequency of orientation-tuned synapses (Chen et al., 2013). Each synapse is assigned an orientation preference, with values being 0° to 360° in steps of 10°. This distribution of orientation preferences to the stimulus-driven synapses at the dendritic tree level followed a Gaussian probability density function wrapped around the unit circle:

$$f(s) = \frac{1}{W\sqrt{2\pi}} \sum_{k=-1}^{1} e^{-\frac{(s-b+2\pi k)^2}{2W^2}}$$

where W is the standard deviation (30°; Chen et al., 2013), s is the synaptic orientation preference and b is the mean of the distribution (apical or basal tree mean orientation preference, ranging from 0° to 90° in steps of 10°). The parameter k controls the wrapping around the unit circle, and takes the values [-1, -0.5, 0, 0.5, 1]. As a result, the mean orientation preference of each dendritic tree is biased towards the chosen mean orientation preference. By implementing excitatory stimulus-driven connectivity in this way, we also emulate the "like-to-like" connectivity motifs seen *in vivo* (as seen in e.g. Ko et al., 2011; Rossi et al., 2020), as (virtual) presynaptic neurons with orientation preferences close to the mean orientation preference of the model neuron are more likely to connect to it, due to being over-represented in the overall pool of possible synapses. Somatic/neuronal orientation preference was evaluated using the approach described in section 2.3.3.

8.2. Biophysical Manipulations

The following manipulations aimed to evaluate somatic output under different sets of conditions:

(1) <u>Sodium (channel) blockage</u>: selectively nullify (set to zero) sodium conductance (g_{Na}) in a designated compartment (e.g. apical tree, specific basal dendritic segments, or soma).

964 (2) Synaptic modulation: selectively alter synaptic conductances (g_{AMPA}/g_{NMDA}) in a designated
965 compartment or dendritic tree.
966 (3) Input manipulation: selectively deactivate specific types of input (excitatory stimulus-
967 driven and background-driven).
968
969 **8.3. Simulation Protocols**

970 All simulations were performed on our High-Performance Computing Cluster (Rocks 7.0) with
971 624 cores and 3.328 TB of shared RAM under CentOS 7.4 OS (Papadopoulos et al., 2003),
972 through the NEURON simulation environment (Hines & Carnevale, 2001). Model neuron
973 output measurements were obtained at a sampling rate of 10 KHz (dt = 0.1 ms).

974 The following simulation protocols were implemented:
975 (1) Iterative paired-pulse protocol (I3P): Used for the evaluation of dendritic non-linearities.
976 Following synaptic silencing and g_{Na} nullification in the entire model neuron excluding the
977 dendritic segment under investigation, a number (1-200, with step 1) of evenly spaced
978 (uniformly distributed) excitatory synapses are synchronously activated (2 pulses at 50 Hz).
979 Voltage at the midpoint of each dendritic segment was recorded to evaluate dendritic non-
980 linear behavior caused by sodium and NMDA spikes.
981 (2) Stimulation protocol: the model is simulated for 2500 ms (2.5 s), with oriented stimulus
982 presentation onset at 500 ms (0.5 s), lasting until the end of the simulation (duration 2 s).
983 (3) Orientation tuning validation protocol: Using the above stimulation protocol, we simulate
984 10 model "neurons" that feature different synaptic location patterns, defining 10 distinct
985 *neuron IDs*. For each one of these neuron IDs, we use 10 different permutations, with
986 different instances of the input spike trains, resulting in 10 different *simulation IDs* for each

neuron ID. Stimuli of 18 different orientations (0° to 170° in steps of 10°) are then presented in separate simulations. The tuning curve is extrapolated by averaging firing rates across simulation IDs for each neuron ID. The overall tuning properties (width, OSI) were then computed through averaging responses across neuron IDs for each stimulus orientation. Neuron IDs with an OSI of less than 0.2 or a tuning width greater than 80° (as determined by a Gaussian fit) are excluded. If more than 20% of neuron IDs do not meet this criterion, the specific parameter combination is considered to not result in orientation tuning. No neurons were excluded based on the preceding criteria in our simulations.

(4) <u>Orientation disparity protocol:</u> To evaluate the contribution of the apical and basal trees in the somatic orientation preference, we keep the mean apical tree orientation preference fixed at 0°, and set the mean basal tree orientation preference to any one of 10 different values (0° to 90° in steps of 10°) (see also section 8.1). Thus, we introduce orientation tuning *disparity* between the two trees, ranging from 0° to 90°. Akin to the orientation tuning protocol, we independently generate 10 different neuron IDs with 10 different simulation IDs for each one and present stimuli as above (section 8.3.3). Orientation preference is then calculated as described above (section 8.3.3). If more than 20% of the neuron IDs are rejected (OSI < 0.2 or tuning width > 80°) for a given degree of orientation tuning disparity, then the model as a whole is deemed to exhibit no orientation tuning for that level of disparity.

In order to determine whether the somatic response follows the mean apical or basal tree preferred orientation most closely, we compute the *expected* orientation preference of each neuron ID; that is, the orientation preference assuming a linear summation of the synaptic inputs. Specifically, we record the assigned orientation preference of all synapses per neuron ID, and then we use Euler's Formula to calculate the expected orientation preference for this neuron ID:

$$E_d = arctan\left(\frac{\sum_i sin(T_i^A) + \sum_j sin(T_j^B)}{\sum_i cos(T_i^A) + \sum_j cos(T_j^B)}\right)$$

Where E_d is the expected orientation preference for a degree of disparity d, i and j are the numbers of stimulus-driven apical and basal synapses respectively, and T^A and T^B are lists of synaptic orientation preferences for the apical and basal trees, respectively. In this particular protocol, a remapping of preferences is required in specific cases (e.g. 180° → 0°) since we are not simulating direction selectivity, projecting orientation preferences into the [-90°, 90°) interval.

(5) Spontaneous activity protocol: Similarly to the orientation tuning validation protocol, we use 50 different neuron IDs with 100 different simulation IDs for each one. Simulations feature no stimulus-driven synaptic activity, leaving only background-driven synapses active.

(6) Ionic intervention protocol: Using 50 neuron IDs with 10 different simulation IDs for each one, prior knowledge of action potential occurrence is obtained via the stimulation protocol (see section 8.3.2; presented stimulus: 0°, corresponding also to the mean apical and basal tree orientation preference), using the 'biological plausible' synaptic distribution (section 8.1). This protocol proceeds similarly to the stimulation protocol (with the notable exception of somatic g_{Na} being set to 0 to prevent backpropagation) until a time before point t_i, which is the time of somatic spike occurrence. At t_i – 3 ms, g_{Na} is set to 0 on either the apical or basal tree dendrites in two separate simulations, until t_i + 1 ms. This manipulation selectively eliminates the contribution of apical or basal dendritic sodium conductances (seen either as depolarization or as dendritic spikes) to the somatic spike. This protocol is repeated for all somatic spikes and the ensuing voltage traces are analyzed to ascertain whether the somatic spikes survived the manipulation. Spikes rendered extinct only when intervening on the apical

tree are labeled as “apically-driven”, while those rendered extinct when intervening on the basal tree are labeled as “basally-driven”. The spikes rendered extinct by either intervention are labeled as “cooperative”. We observed no cases of somatic spikes failing to become extinct in at least one of the two interventions while using this protocol.

(7) Synaptic intervention protocol: This protocol proceeds similarly to the ionic intervention protocol (note that somatic g_{Na} is not set to 0 in this protocol), with two main differences: (a) the intervention reduces stim-driven AMPA and NMDA synapse conductances on either the apical or basal tree by a specific percentage (e.g. 50%, 90% etc.), rather than setting g_{Na} to 0, (b) the window of the intervention changes from [t_i – 3 ms until t_i + 1 ms] to [t_i – 30 ms until t_i +10 ms] (10x increase in window size). This was done to compensate for the relatively low peak activation frequencies of stim-driven synapses (0.3 Hz).

(8) Ablation protocol: Apical dendrites and their corresponding synapses are not generated under this protocol, simulating a neuron 1 day after laser ablation of the apical dendrites (Park et al., 2019). As firing rates greatly increase (more than 10-fold increase) under these conditions, basal AMPA and NMDA synaptic conductances are reduced by 45% to bring the firing rate back down to expected levels.

8.4 Two-Photon Microscopy

(1) Animals in Experiments: All experimental protocols were approved by Brigham and Women’s Hospital (BWH) Institution Animal Care and Use Committee. Male and female wild-type (C57BL/6) mice were purchased from The Jackson Laboratory and bred for experiments. A total of 2 mice were used in these experiments.

(2) Chronic Window Implantation and Sparse Labeling: Viral vectors were purchased from

1057 Addgene. For viral injections and chronic window implantation, 6-10 week old wild type
1058 C57BL/6 mice (both male and female) were anesthetized with isoflurane (1-1.5%). The depth
1059 of anesthesia was assessed via monitoring breathing rates. Meloxicam (2.5mg/kg) and
1060 Buprenorphine (0.1mg/kg) were administered subcutaneously every 12 hours following the
1061 surgical procedure for 2 days. A headpost was implanted on the skull and a 3mm diameter
1062 craniotomy was made over the visual cortex of the left hemisphere. The craniotomy was
1063 centered 2.7mm lateral to the midline and 1.5mm posterior to the bregma. To sparsely label
1064 pyramidal neurons with GCaMP6s, a mix (~90 nl per site, up to 2 sites) of diluted CamKII-CRE
1065 (AAV1, diluted 80,000X) and flex-GCaMP6s (AAV5, diluted up to 2X) was injected slowly over
1066 5 minutes per penetration using a Drummond Nanoject III. Up to two penetrations ~0.5mm
1067 apart on average were performed per craniotomy. After the viral injection, a round coverslip
1068 was fitted to the craniotomy and sealed with vetbond and dental cement. Most chronic
1069 windows in our hands remain clear for 2-3 months. 2-photon imaging was performed on week
1070 3-4 following viral injection, at which time GCaMP6s expression was optimal.
1071 (3) <u>In vivo calcium imaging of sparsely labeled neurons:</u> Three to four weeks after the
1072 injection, each GCaMP6s expressing mouse was sedated with Fentanyl (0.5 mg kg^{-1}) and
1073 Dexmedetomidine (0.5 mg kg^{-1}) (Mrsic-Flogel et al., 2007) for imaging experiments. A stable
1074 level of anesthesia was confirmed by stable breathing rate and lack of movement. Neuronal
1075 and dendritic calcium activity was recorded from L2/3 pyramidal neurons in V1. We chose
1076 neurons with 1 to 3 primary basal dendritic segments clearly visible up to their primary
1077 branching point on the same plane with the soma. Apical dendrites were not present in the
1078 focal plane during recording. Mice were in the dark during the imaging process and their
1079 spontaneous firing rate was recorded. Images were acquired at ~7.3 frames/sec using an
1080 Ultima IV microscope in spiral scanning mode with a 25X 1.0 NA Nikon objective (5-30mW

laser power, 900 nm). Recordings lasted for 283 s (2750 frames). The size of the recording FoV was 103 μm^2, and the pixel size was 0.201 μm^2. 12 pyramidal neurons were imaged, and 11 of these were selected for analysis. The final neuron was not selected due to an insufficient number of basal dendritic segments being positively identified as belonging to said neuron following visual inspection of a z-stack image.

8.5. Data Analysis

Data analysis of both modeling and two-photon imaging experiments was performed through Python 3.8+, using publicly available libraries as well as custom-made scripts and functions. The latter include:

(1) Dendritic Spike Detection: Dendritic sodium spikes were identified via a detection algorithm that identified depolarizations exceeding a -20 mV threshold. For the identification of NMDA spikes in the I3P experiments (see section 8.3.1) we located the inflection points (points where the second derivative is zero) of the voltage trace after the second pulse. As the NMDA spike exhibits a voltage plateau, 2 or more inflection points indicate an NMDA spike. As our voltage measurements are not continuous and the I3P protocol does not feature noise, it is unlikely to encounter a measurement point at which the second derivative is exactly zero. Thus, we assume an inflection point exists at some recording point P_n if and only if $(P_{n-1} \cdot P_{n+1}) < 0$, where P_{n-1} and P_{n+1} refer to existing points in the second derivative of the voltage trace, immediately preceding and following the theorized inflection point.

(2) Quantification of Dendritic Nonlinearities: Using data from the I3P experiments, we calculated the maximum amplitude of dendritic segment depolarization per synapse count. A linear input-output curve is then generated, extrapolating from the response of the dendritic

segment to a single synaptic input (unitary response). This curve is compared to the actual response of the dendritic segment to increasing input in an “Expected vs. Actual” plot, thus coarsely characterizing the integration mode of the dendritic segment. The integration mode of the dendritic segments was quantified in detail using the Nonlinearity Relative to Linear Extrapolation (NRLE) metric (Behabadi et al., 2012), which is defined as the maximum ratio of actual to expected neuronal output signal. An NRLE value of less than 1 denotes a sub-linear dendritic segment, NRLE of exactly 1 indicates a linear dendritic segment and NRLE values over 1 characterize a dendritic segment as supra-linear. The non-linearity threshold of all dendritic segments was also calculated, measured as the minimum number of synapses required to elicit the corresponding electrogenic event (sodium or NMDA dendritic spike).

(3) Two-Photon Imaging Data Analysis: Recordings are motion corrected via the suite2p software (Pachitariu et al., 2016) to accurately extract fluorescence values from dendritic segments. In the case of somatic activity data, we use the original video, as motion correction is not necessary at the level of magnification used. Using the Fiji ImageJ software (Schindelin et al., 2012), ROIs are manually defined, using a maximum intensity z-stack as a reference image. Dendritic segments are identified as belonging to the cell of interest via visual inspection of a z-stack recording. Each dendritic segment is broken up into multiple ROIs. Only one ROI is defined for the soma. We completely avoid areas where there is an overlap of the cell of interest with nearby dendrites/axons of cells from outside the field of view. Dendritic ROIs are slightly wider than the dendritic segments themselves, to partially account for misplacement of the ROI or uncorrected movement (drift) of the dendrite. 4 equal-sized circular ROIs are also defined in areas where no visible dendritic segments or somata can be found to calculate the background fluorescence level.

(4) Calcium Trace Processing: Raw calcium fluorescence data is normalized via a moving

1128 window average of the fluorescence trace (window size of 20 s), subtracting F_0 from it
1129 (defined as the average of the 20% lowest fluorescence values of said moving 20s window),
1130 then dividing by the same value (F0), finally producing a normalized $\Delta F/F_0$ value. These $\Delta F/F_0$
1131 values were significantly different from the background $\Delta F/F_0$ as calculated from the 4 circular
1132 reference ROIs (cross-correlation test; $p < 0.05$; no manually-defined ROIs were excluded
1133 through this process).
1134 (5) Calcium Event Detection: Calcium events are detected via a simple dual-threshold
1135 approach: a calcium event is registered when the ΔF/F value exceeds the 93.5^{th} percentile at
1136 the same time as the derivative of the ΔF/F value exceeds the 67th percentile. These percentile
1137 values were calculated via trial-and-error, attempting to match the expected firing frequency
1138 of a neuron (soma) under spontaneous activity conditions (approximately 0.2 Hz; Haider et
1139 al., 2013). To ensure that the algorithm returns true events rather than random noise, we
1140 performed an Event-Triggered Average (ETA) analysis. We extracted all of the detected event
1141 waveforms, centered them on the time of detection, and averaged across waveforms. We did
1142 this separately for somatic and dendritic events (*Supplementary Figure 2C)*, as well as for each
1143 animal separately (*Supplementary Figures 4A, 4B*). Calcium event-triggered averaging of the
1144 processed fluorescence signal yields the expected temporal profile, indicating that these
1145 events are not likely to represent noise.
1146 (6) Generation of "fluorescence-like" traces from model voltage traces: 50 neuron IDs were
1147 simulated with 100 simulation IDs each, using the "biologically plausible" configuration under
1148 the spontaneous activity protocol, in order to closely match the properties of the real neurons
1149 under spontaneous activity conditions. Next, we ran a spike detection algorithm to find all
1150 somatic and dendritic spiking events. We binarized the traces, using 1 for spike peaks and 0
1151 otherwise. We then convolved these binarized traces with a GcaMP6s kernel function of our

own design:

$$F(t) = -s\left(e^{-\frac{t-t_0}{t_r}} - e^{-\frac{t-t_0}{t_d}}\right)$$

Where t is time (in ms), s is a scaling factor (s ≈ 0.5714), t0 is the time of the event, t_r is the rise time (t_r = 74 ms) and t_d is the decay time (t_d ≈ 401.45 ms). The output of the function is unitless, representing fluorescence. With these parameters, our kernel function has an actual rise time constant of 194.225 ms, with output values decaying by ~52.11% within 0.6 s (*Supplementary Figure 3A*). These values closely match experimentally observed values for GCaMP6s (*Supplementary Figure 3B;* Chen et al., 2013). The ensuing fluorescence traces were then downsampled to a dt of 0.138 s (~7.25 Hz) from the original dt of 0.1 ms (10 KHz), to emulate the sampling rate of our two-photon calcium fluorescence imaging. The transformed traces were then processed by the same pipeline as true calcium fluorescence data (see sections 8.5.4 and 8.5.5).

(7) <u>Analysis and comparison of true vs "generated" fluorescence data:</u> Voltage traces from the soma and basal dendritic segments were converted into approximations of two-photon fluorescence traces (see section 8.5.6) to allow a direct comparison with in vivo calcium imaging data that were collected under similar conditions. Significant fluorescence increase "events" were identified for both datasets using a custom detection algorithm (see section 8.5.5). To ensure that the algorithm detects true events rather than noise in the two-photon signal, we performed an event-triggered averaging (ETA) analysis of trace segments centered on the event onset timepoint (see section 8.5.5; 1131 dendritic events, 96 somatic events across all 11 neurons and their respective dendritic ROIs). The results of this analysis indicate that random noise is unlikely to be the cause of the detected events, as there is a marked increase in fluorescence intensity at the time of event onset for all detected events

1176 (*Supplementary Figure 2D, Supplementary Figures 4&5*) which persists over time.

1177 Next, in order to infer the relationship between basal and somatic events, we looked at their
1178 relative timing differences. Using dendritic events as the starting point, we paired each
1179 dendritic event with the most temporally proximal somatic event, and computed the time
1180 difference between the two for each event pair (measured in imaging frames, each lasting
1181 approximately 138 ms). Using the same approach, we measured the fraction of somatic-
1182 dendritic event pairs in our model and compared them to the in vivo data. Event pairs
1183 featuring a temporal distance of zero (occurring within the same frame) were excluded as
1184 they are most likely to represent backpropagating events (excluded event pairs: model:
1185 219,291/245,717 event pairs, 89.25%; in vivo: 29,143/237,572 event pairs, 12.27%; difference
1186 attributed to a lack of noise-related fluctuations in the model data compared with the in vivo
1187 data). The resulting distributions (*Supplementary Figures 2E&F*) show that in both the model
1188 and in vivo data local dendritic events can be generated independently of somatic events.
1189 Paired events separated by more than 4 recording frames (~552 ms) are highly unlikely to be
1190 the result of backpropagation, even when considering the slow kinetics of the calcium sensor.
1191 Moreover, the somatic events that are preceded by basal dendritic events are similar in
1192 proportion between datasets (*Supplementary Figures 2E&F*, red bins: 48.79% model, 48.12%
1193 actual when including all event pairs with a non-zero timing difference; 24.3% model, 27.8%
1194 actual when including only event pairs with an absolute timing difference >4 recording
1195 frames).

1196 To mitigate the risk that the in vivo findings are the result of noise or random chance, we
1197 constructed a null distribution of timing differences for the in vivo data by independently
1198 circularly shuffling the time-series data from the somatic and various dendritic segment ROIs

1000 times, and then re-computed the timing differences. We then compared the actual data with the null distribution data using the two-sample Kolmogorov-Smirnov (KS) test, finding that the two distributions of timing differences were significantly different (*Supplementary Figure 4C*; test statistic ~0.105, $p << 0.05$), whereas a similar analysis of completely randomly generated event timings would results in identical (not statistically different) distributions for event pair timing differences. It is important to note that the analyses herein are inherently subject to the noisy nature of the recordings, the limitations of the slow kinetics of the calcium indicator, the low temporal resolution of the recording (frame time of ~138 ms), as well as the possibility of undetected events.

(8) <u>Electrotonic constant calculation:</u> The electrotonic constants (mentioned also in text as "ELC") of all dendritic segments were calculated using the formula from van Elburg & van Ooyen (2010):

$$\lambda_i = \sqrt{\frac{b_i r_m}{2r_a}}$$

Where i refers to the dendritic segment, λ_i is the electrotonic length constant, b_i is the radius of the branch, r_m is the specific membrane resistance and r_a is the intracellular resistivity. To derive the final value (electrotonic constant or "ELC"), we divide the length of each dendritic section by its corresponding λ_i .

(9) <u>Quantification of Dendritic Impact on Somatic Output:</u> To ensure relative equivalence between the levels of activity in each dendritic branch, we start by providing each dendritic branch the minimum amount of synaptic input required such that each one features either an EPSP of approximately 20 mV (19.78 ± 0.98 mV; *Figure 5A&B, Supplementary Figure 8C&D*), or a dendritic sodium spike (*Supplementary Figure 8A&B, Supplementary Figure 8E&F*). Only

1222 one dendritic branch received inputs each time, and somatic (but not dendritic) sodium
1223 channels had their conductance set to zero in order to accurately measure signal attenuation.
1224 After measuring the attenuation of this EPSP or spike at the soma, we attempted to describe
1225 it as a function of different morphological and electrophysiological parameters by dividing the
1226 attenuation observed at the soma by the corresponding value of the parameter for the given
1227 dendritic branch. The parameters used were dendritic length, dendritic diameter, distance of
1228 dendritic segment from the soma, dendritic volume, dendritic path volume (defined as the
1229 sum of the volumes of all dendritic segments linking the given dendrite with the soma,
1230 including the volume of the given dendrite) and dendritic electrotonic constant (see section
1231 8.5.8). Values can then be compared across dendrite types (apical vs basal) for each
1232 parameter by performing Welch's t-test. We also performed a similar analysis using the
1233 dendritic sodium spiking threshold (*Figure 1E&F*) instead of dendritic signal attenuation, with
1234 the same morphological and electrophysiological parameters as above (*Figure 5C&D*). To
1235 ensure fairness of comparisons, we excluded from these analyses any dendrites belonging to
1236 the apical trunk (4/43 apical dendritic segments), any apical dendrites with atypical properties
1237 (4/43 apical dendritic segments featuring a relatively high sodium spiking threshold for their
1238 morphology, produced as a side-effect of the 3d reconstruction; lengths: 16.2±10.5 µm;
1239 diameters: 0.711±0.027 µm), as well as any apical dendrites whose value for the parameter
1240 under examination was outside 3 standard deviations of the basal dendrite mean for the same
1241 parameter. Note that the qualitative results of the analysis did not change even if no dendrites
1242 were excluded.
1243 (10) <u>Relationship of Branch Order and Distance with Signal Attenuation:</u> To check whether
1244 apical and basal dendrites feature different levels of attenuation for 20 mV EPSPs or dendritic
1245 sodium spikes (see section 8.5.9), we compared the levels of attenuation for these events

between basal dendrites and apical dendrites of high branch order (> 3) or high distance from the soma (> 182.7 µm, equivalent to the maximum distance of any basal dendritic segment from the soma). We excluded basal dendritic segment #3 (root branch of the bifurcating basal dendrite) from the analysis, since it featured extremely low attenuation values because of additional current received from its child branches. After isolating the EPSP and spike attenuation data from the dendrites that matched the above criteria, we compared the resulting sets of values using Welch's t-test.